The Astrophysical Journal, 932:27 (15pp), 2022 June 10 https://doi.org/10.3847/1538-4357/ac6bed


# The Redshift Evolution of Ultraluminous X-Ray Sources out to $z \sim 0.5$: Comparison with X-Ray Binary Populations and Contribution to the Cosmic X-Ray Background

R. Scott Barrows[1], Julia M. Comerford[1], Daniel Stern[2], and Marianne Heida[3]
[1] Department of Astrophysical and Planetary Sciences, University of Colorado Boulder, Boulder, CO 80309, USA; Robert.Barrows@Colorado.edu
[2] Jet Propulsion Laboratory, California Institute of Technology, 4800 Oak Grove Drive, Pasadena, CA 91109, USA
[3] European Southern Observatory, Karl-Schwarzschild-Str. 2, D-85748 Garching b. München, Germany
*Received 2021 October 29; revised 2022 April 15; accepted 2022 April 28; published 2022 June 13*

## Abstract

Ultraluminous X-ray sources (ULXs) are thought to be powerful X-ray binaries (XRBs) and may contribute significantly to the redshift-dependent X-ray emission from star-forming galaxies. We have assembled a uniform sample of 259 ULXs over the redshift range $z = 0.002$–$0.51$ to constrain their physical nature and their contribution to the cosmic X-ray background. The sample is constructed by crossmatching galaxies from the Sloan Digital Sky Survey with the Chandra Source Catalog and selecting off-nuclear X-ray sources after applying astrometric corrections. The fraction of contaminants is ∼30% and shows no evolution with redshift. The host-galaxy star formation rates (SFRs) are systematically elevated relative to the parent sample when matched in host stellar mass. The specific SFRs suggest a slight preference for high-mass XRBs, and the X-ray luminosity scaling relations with host-galaxy stellar mass and SFR indicate that the highest-redshift sources represent relatively luminous XRB populations that dominate their host-galaxy X-ray emission. The fraction of galaxies hosting at least one ULX of a given luminosity increases with redshift over the full range of our sample, as expected if ULXs are preferentially found in galaxies with high SFRs and low metallicities. At $z \sim 0.5$, the ULX X-ray flux is consistent with the X-ray emission from star-forming galaxies. Moreover, ULXs may account for up to ∼40% of the integrated flux from XRBs in the normal galaxy population out to $z \sim 0.5$, suggesting they may contribute significantly to the overall ionizing radiation from galaxies.

*Unified Astronomy Thesaurus concepts:* X-ray binary stars (1811); Star formation (1569); Neutron stars (1108); Stellar mass black holes (1611); Metallicity (1031); Ultraluminous x-ray sources (2164); X-ray sources (1822)

*Supporting material:* machine-readable table

## 1. Introduction

Ultraluminous X-ray sources (ULXs) are defined as X-ray sources in off-nuclear regions of galaxies with observed fluxes that (assuming isotropic emission) correspond to luminosities exceeding the theoretical Eddington limit for accretion onto stellar-mass compact objects (for a review, see Kaaret et al. 2017). The adopted lower-luminosity limits of ULX categorization vary from $L_X = 2 \times 10^{38}$ erg s$^{-1}$ (Eddington limit for a 1.4 $M_\odot$ neutron star) to $L_X = 3 \times 10^{39}$ erg s$^{-1}$ (Eddington limit for a ∼20 $M_\odot$ black hole; BH). Super-Eddington accretion onto stellar remnants is considered the most likely explanation for ULXs (e.g., King et al. 2001; Gladstone et al. 2009; Sutton et al. 2013) and has been confirmed in several nearby cases via neutron star pulsed X-ray emission (Bachetti et al. 2014; Fürst et al. 2016; Israel et al. 2017a, 2017a; Chandra et al. 2020) and resonance features due to a magnetic field (Brightman et al. 2018). A significant fraction of other well-studied nearby ULXs observed by the Nuclear Spectroscopic Telescope Array show hard X-ray excesses that may also be due to pulsation (e.g., Bachetti et al. 2013; Walton et al. 2013; Mukherjee et al. 2015; Walton et al. 2015; Luangtip et al. 2016; Walton et al. 2018), and super-Eddington accretion onto a neutron star has been observed to produce an X-ray luminosity of up to $L_X \sim 2 \times 10^{41}$ erg s$^{-1}$ (Israel et al. 2017a). On the other hand, more luminous off-nuclear X-ray sources are referred to as hyperluminous X-ray sources (HLXs) and are more likely associated with accretion onto intermediate or supermassive BHs (IMBHs and SMBHs, respectively) with masses of $M_{\rm BH} > 1000\,M_\odot$ (e.g., King & Dehnen 2005; for a review see Mezcua 2017).

If ULXs are powered by accretion onto stellar remnants, then they are likely a subset of the X-ray binary (XRB) population in which the accretors are either neutron stars or BHs in a gravitationally bound system with a donor star that supplies the accreted mass (for a review of Galactic XRBs, see Remillard & McClintock 2006). XRBs with donor star masses of $<(>)$ 10 $M_\odot$ are referred to as low(high)-mass XRBs (LMXBs and HMXBs, respectively), and the mass is transferred from the donor star via Roche-lobe overflow or from stellar winds. Given that massive stars can provide more material for accretion, the most-luminous ULXs are more likely powered by HMXBs with mass-transfer rates that can exceed the Eddington limit (e.g., Pavlovskii et al. 2017), though geometrical beaming along the line of- sight can significantly augment the observed luminosities (e.g., Middleton & King 2017).

The long-lived donor stars of LMXBs mean that their global emissivity is most strongly correlated with their host-galaxy total stellar masses (e.g., Gilfanov 2004; Boroson et al. 2011). On the other hand, the emissivity of HMXBs is tied to their host-galaxy star formation rates (SFRs) that trace the formation of massive and short-lived donor stars (e.g., Grimm et al. 2003; Ranalli et al. 2003; Hornschemeier et al. 2005; Mineo et al. 2012). Because the total stellar masses and SFRs of galaxies

evolve with redshift (e.g., Madau & Dickinson 2014, and references therein) and their metallicities may have a significant impact on the form of this evolution (e.g., Fornasini et al. 2019, 2020), the formation frequency and nature of XRBs will also evolve with redshift. This evolution has been empirically constrained out to high redshifts through X-ray stacking (e.g., Basu-Zych et al. 2013; Lehmer et al. 2016; Aird et al. 2017), and comparison with stellar population synthesis models (Fragos et al. 2013b; Madau & Fragos 2017) suggests that HMXBs dominate the XRB emissivity at high redshifts, while LMXBs dominate after $z \sim 2$ due to increasing galaxy metallicities. Moreover, aggregate XRB populations produce most of the X-ray emission from normal (i.e., without active galactic nuclei, hereafter AGNs) galaxies (e.g., Lehmer et al. 2012) and may contribute up to $\sim 20\%$ of the cosmic X-ray background (CXB) when integrated out to $z = 10$ (e.g., Dijkstra et al. 2012).

However, whether or not ULXs follow a similar evolutionary path is currently not clear. Indeed, ULXs dominate the point-source luminosities of normal star-forming galaxies (e.g., Colbert et al. 2004; Fabbiano 2006), and the CXB may therefore be affected by the redshift evolution of ULXs. This contribution has strong implications for several areas of modern astrophysics, including constraints on the sources of interstellar medium (ISM) heating and feedback (e.g., Pakull et al. 2010; Soria et al. 2014; López et al. 2019), empirical laboratories for extreme mass accretion rates and/or geometrical beaming, and for the progenitors of gravitational-wave sources produced by the coalescence of BHs more massive than known Galactic stellar remnants (e.g., Abbott et al. 2016; Nitz et al. 2020).

Furthermore, some ULXs may alternatively be low-luminosity AGNs in the tidally stripped cores of galaxies that merged with the host galaxy and are wandering within its gravitational potential (e.g., Farrell et al. 2009; Comerford et al. 2015). Given that ULX optical counterparts are typically much fainter than expected for the stripped bulges of massive galaxies, in the AGN scenario they likely represent IMBHs from dwarf galaxies (e.g., King & Dehnen 2005; Wolter et al. 2006; Feng & Kaaret 2009; Jonker et al. 2010; Mezcua et al. 2015; Barrows et al. 2019). The IMBH scenario may also be possible if it formed in situ within a dense stellar system, such as a globular cluster (e.g., Sigurdsson & Hernquist 1993; Miller & Hamilton 2002; Maccarone et al. 2007) or a compact star cluster (e.g., Ebisuzaki et al. 2001).

While ULXs in the nearby universe have been studied extensively (Colbert & Ptak 2002; Swartz et al. 2004; Liu & Mirabel 2005; Liu & Bregman 2005; Liu 2011; Swartz et al. 2011; Walton et al. 2011; Gong et al. 2016; Earnshaw et al. 2019; Kovlakas et al. 2020; Inoue et al. 2021; Walton et al. 2022), their properties past $z \sim 0.05$ are poorly constrained. Hornschemeier et al. (2004) originally identified 10 intermediate-redshift ULX candidates[4] from the Chandra Deep Field−North and the Chandra Deep Field−South ($z = 0.038$–$0.232$, with a median of $z \sim 0.11$). Lehmer et al. (2006) identified 15 additional ULX candidates by also incorporating the Extended Chandra Deep Field−South ($z = 0.038$–$0.298$, with a median of $z \sim 0.14$). Both studies found tentative evidence that the fraction of galaxies hosting ULXs is larger at intermediate redshifts compared to locally. Mainieri et al. (2010) subsequently identified seven new ULX candidates in the Cosmic Evolution Survey (COSMOS; Scoville et al. 2007) field ($z = 0.072$–$0.283$, with a median of $z \sim 0.13$), finding a smaller occupation fraction that suggests a weaker redshift dependence. In this paper, we build upon these results by studying the redshift evolution of ULXs using a large and uniformly constructed sample that ranges from the local universe out to intermediate redshifts ($z \sim 0.002$–$0.5$) for the first time.

This paper is structured as follows: In Section 2 we describe the steps taken to create the sample, in Section 3 we estimate the fraction of unknown background or foreground contaminating X-ray sources, in Section 4 we estimate the host-galaxy properties, in Section 5 we compare the ULXs with XRB populations, in Section 6 we examine the ULX occupation fraction, in Section 7 we determine the contribution of ULXs to the CXB, and in Section 8 we present our conclusions. Throughout we assume a flat cosmology defined by the nine-year Wilkinson Microwave Anisotropy Probe observations (Hinshaw et al. 2013): $H_0 = 69.32$ km Mpc$^{-1}$ s$^{-1}$ and $\Omega_M = 0.2865$.

## 2. Building the Sample

Our procedure for building the sample of ULX candidates is as follows: selection of the initial galaxy sample (Section 2.1) and the initial X-ray source sample (Section 2.2), spatial crossmatch of the galaxies and X-ray sources (Section 2.3), selection of spatially offset X-ray sources (Section 2.4), application of X-ray luminosity thresholds that target ULXs (Section 2.5), and removal of AGNs and known contaminants (Section 2.6). The basic properties of the final sample are summarized in Section 2.7, and the effects of source confusion are discussed in Section 2.8.

### 2.1. Galaxy Selection

The initial galaxy sample is derived from the catalog of Sloan Digital Sky Survey (SDSS) detections in Data Release 16 (DR16; Ahumada et al. 2020) that are classified as `Galaxy` and with measured photometric redshifts ($z_{\rm phot}$). We remove all detections that were flagged as saturated by the SDSS pipeline. If a galaxy is in the SDSS spectroscopic sample, then we adopt the spectroscopic redshift ($z_{\rm spec}$) as the final redshift value ($z$). Otherwise, we query the NASA Extragalactic Database (NED) for a spectroscopic redshift using a crossmatch radius of 5′. If multiple source matches are found, we take the closest match. Furthermore, if a matched source has multiple values of $z_{\rm spec}$, then the value with the smallest uncertainty is used.

If no value of $z_{\rm spec}$ is available, then that of $z_{\rm phot}$ is used. Values of $z_{\rm phot}$ were derived by the SDSS pipeline based on a training sample of galaxies with spectroscopic redshifts and with similar colors and $r$-band magnitudes.[5] The $z_{\rm phot}$ accuracy of the parent galaxy sample (as quantified by comparison to the $z_{\rm spec}$ values) is illustrated in the top panel of Figure 1. The bottom panel of Figure 1 demonstrates how the photometric redshift errors ($E_{z_{\rm phot}}$; described in Scranton et al. 2005) are generally reliable tracers of the true accuracy as quantified by the lower and upper 68.3% bounds around the one-to-one relation ($\sigma_{\rm z,lo}$ and $\sigma_{\rm z,hi}$, respectively). However, on average the $E_{z_{\rm phot}}$ values are smaller than both $\sigma_{\rm z,lo}$ and $\sigma_{\rm z,hi}$. Therefore, to

[4] The term "candidate" is used because a fraction of ULXs is expected to be unrelated background or foreground sources. Spectroscopic redshifts of the accreting sources are the best means of confirming or rejecting association with the host galaxy.

[5] https://www.sdss.org/dr12/algorithms/photo-z/

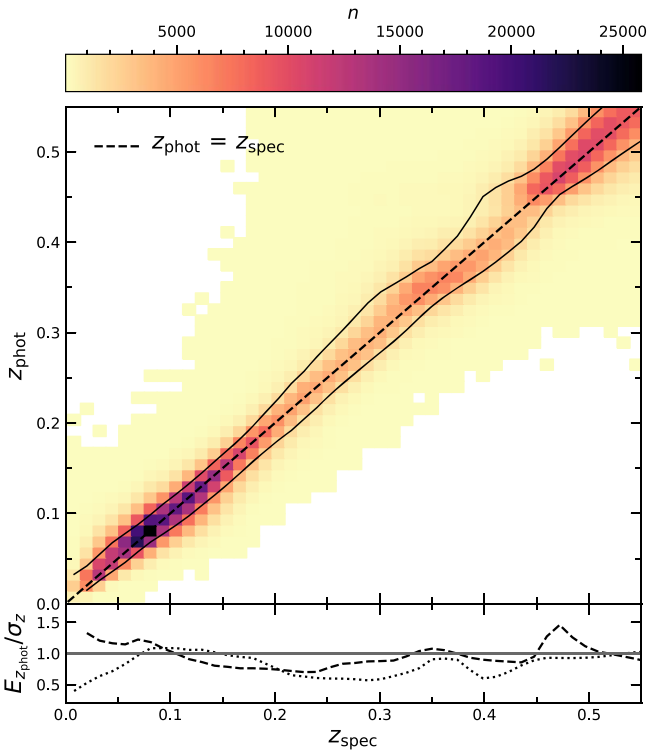


**Figure 1.** Top: photometric redshifts ($z_{phot}$) against spectroscopic redshifts ($z_{spec}$) for the subset of the initial galaxy sample (Section 2.1) with $z_{spec}$ values. The plotted redshift range encompasses our final sample (Section 2.7). Number densities ($n$) are shown for $n > 20$. The solid lines bound the 68.3% confidence lower and upper intervals ($\sigma_{z,lo}$ and $\sigma_{z,hi}$, respectively) around the one-to-one relation (dashed). Bottom: ratio of the photometric redshift error ($E_{z_{phot}}$) to $\sigma_{z,lo}$ (dashed) and to $\sigma_{z,hi}$ (dotted). The horizontal line indicates $E_{z_{phot}} = \sigma_z$. Both $\sigma_{z,lo}$ and $\sigma_{z,hi}$ are overall accurately traced by $E_{z_{phot}}$ though they are on average larger. Therefore, we adopt $\sigma_{z,lo}$ and $\sigma_{z,hi}$ as our final $z_{phot}$ errors.

avoid systematic underestimates of $E_{z_{phot}}$, for the $z_{phot}$ errors we use $\sigma_{z,lo}$ and $\sigma_{z,hi}$.

### 2.2. X-Ray Source Selection

The High Resolution Camera and the Advanced CCD Imaging Spectrometer on the Chandra X-Ray Observatory provide the best spatial resolution of current X-ray telescopes (Weisskopf et al. 2000) and are therefore optimal for identifying off-nuclear X-ray sources out to intermediate redshifts. To obtain the most comprehensive list of robust source detections from Chandra, we use the Chandra Source Catalog (Evans et al. 2010) Version 2 (CSC2) Master Sources as our initial sample of X-ray sources.

Because ULXs are defined as point sources, we omit X-ray sources with a 68% lower confidence limit on the $1\sigma$ major axis extent that is greater than the point-spread function (PSF) $1\sigma$ radius at the source position. Because each Master Source from the CSC2 can be in multiple observations (OBSIDs), we compute the PSF as the mean value obtained from the PSF maps of each OBSID in the "best" Bayesian block of observations.[6] We further remove any Master Sources flagged as extended (`extent_flag=TRUE`) by the CSC2 pipeline.[7]

[6] Each Bayesian block contains observations with a constant photon flux (Scargle et al. 2013), and the block with the largest combined exposure time is the "best" block: http://cxc.harvard.edu/csc2/data_products/master/blocks3.html.

[7] https://cxc.harvard.edu/csc/columns/flags.html

### 2.3. Matching X-Ray Sources to Galaxies

The parent galaxy sample is the subset of the initial galaxy sample (Section 2.1) that is within the CSC2 footprint. Matches between the parent galaxy sample and the X-ray source sample (Section 2.2) are based on their world coordinates. The SDSS galaxy positions are defined by the $r$-band photometric centroids, and the coordinates of each X-ray source are based on the CSC2 Maximum Likelihood Estimation.[8]

We require that each X-ray source centroid is within one Petrosian radius ($r_{petro}$; measured by the SDSS pipeline) of a galaxy centroid. We remove any galaxies with Petrosian magnitudes fainter than $r = 21$ as the Petrosian radii become significantly less accurate above that threshold. Multiple X-ray sources may satisfy this criterion for a single galaxy. Even though radii of $2 \times r_{petro}$ provide the optimal combination of maximizing the integrated galaxy flux while minimizing sky noise (e.g., Graham et al. 2005), we observe that X-ray sources with angular offsets $>1 \times r_{petro}$ are significantly more likely to have optical counterparts detected in the SDSS imaging (see Section 2.6). Because these optical detections are likely associated with external galaxies (either interacting or background galaxies) and hence do not satisfy the traditional definition of ULXs, we retain the upper angular offset threshold of $1 \times r_{petro}$ to exclude them. This procedure yields 14,820 unique matches between X-ray sources and galaxies.

While the Petrosian radii do not account for the apparent elliptical profiles of inclined galaxies, they are more robust than the SDSS exponential model ellipticities, particularly for the fainter galaxies in the parent galaxy sample. However, to quantify the impact of galaxy inclinations on our selection, we scale the exponential model major and minor radii to yield an elliptical area that equals the circular area defined by the Petrosian radius. The number of ULX candidates selected based on the elliptical galaxy profiles is 97% of the number selected based on the circular galaxy profiles. Furthermore, out of our sample selected using the Petrosian radius, 95% would be selected using the corresponding elliptical profiles. We correct our estimates of the ULX occupation fraction (Section 6) and CXB contribution (Section 7) for the 5% that may be outside of the galaxy profile ellipse.

### 2.4. Selection of Spatially Offset X-Ray Sources

To obtain estimates of the relative astrometric accuracy between the galaxy and X-ray source positions, we follow the procedure outlined in Barrows et al. (2016, 2019). Here we reiterate the basic steps: We first identify significantly detected sources ($>3\sigma$) in the SDSS $r$-band images using `Source Extractor` (Bertin & Arnouts 1996) and in the Chandra images using `wavdetect` (as part of the Chandra `Interactive Analysis of Observations` software; `CIAO`) and a probability threshold of $10^{-8}$. We then filter out unreliable SDSS detections (sources at frame edges and blended sources) and extended sources from both source lists. The host galaxies and candidate off-nuclear X-ray sources are excluded from the source lists to produce astrometric corrections that are independent of the spatial offsets being tested. Matched pairs of sources between the `Source Extractor` and `wavdetect` lists are identified within a $2''$ threshold radius.

Translational corrections along the R.A. and decl. are computed as the mean offset between the final matched source

[8] https://cxc.harvard.edu/csc/columns/positions.html

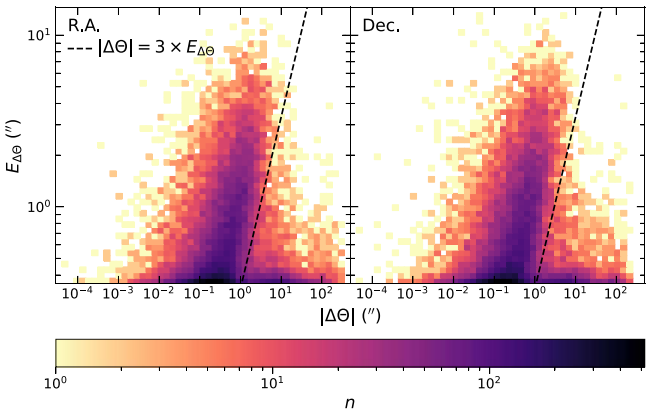


**Figure 2.** Angular offset uncertainty between the X-ray source and the galaxy centroid ($E_{\Delta\Theta}$) against the angular offset ($\Delta\Theta$) along the R.A. (left) and decl. (right) dimensions for the sample of matched galaxy and X-ray source pairs (Section 2.3). The dashed line indicates $\Delta\Theta = 3 \times E_{\Delta\Theta}$ (angular offset criteria used for ULX candidate selection; Section 2.4).

lists after iteratively rejecting matched pairs that are outliers by more than $1.5\sigma$. While astrometric corrections that include a term accounting for rotation and scale factors are more general, they require a large number of matched pairs that are distributed evenly throughout the images for accurate solutions. Because this is not possible for the majority of our sample (the median number of matched pairs is three), for uniformity we do not include this extra term when computing corrections. To quantify the impact of this choice on our results, for the subset with four or more matched pairs we compare the translation-only corrections to those that include a rotation and scale factor term (computed using `wcsmatch` within `CIAO`). We find that the differences in the derived X-ray source positional corrections are negligible and have no effect on the specific ULX candidates selected.

The relative astrometric uncertainties are computed from the quadrature sum of the errors on the source centroids in the final matched list. If no matches are found between a pair of images, then the translational corrections are set to zero, and the astrometric uncertainties are set to the quadrature sum of the absolute astrometric errors from the SDSS (0.″035) and Chandra (0.″8).

The transformations are computed between the SDSS *r*-band image and each Chandra OBSID in which the X-ray source is detected, and the final corrections between a galaxy and X-ray source position are the error-weighted averages of the astrometric corrections between each of the individual image pairs. These corrections are then applied to each X-ray source to put them in the SDSS reference frame. The uncertainties on those final transformations are the standard error of the weighted mean. Then we reapply the step requiring corrected X-ray source positions to be within one Petrosian radius of the galaxy centroid (Section 2.3).

The uncertainty of the X-ray source position relative to the galaxy centroid is the quadrature sum of the final relative astrometric uncertainties, the X-ray source centroid uncertainty, and the galaxy centroid uncertainty. These uncertainties correspond to $1\sigma$ confidence intervals and are computed separately for both the R.A. and decl. Spatially offset X-ray sources are selected as being offset from the host-galaxy centroid by $\geqslant 3$ times the offset uncertainty along either the R.A. or decl. (Figure 2).

We also remove galaxies for which offsets cannot be reliably measured. These are based on a visual inspection and consist of galaxies for which the SDSS photometric detection is not located at the galaxy nucleus, galaxies with dust lanes that may affect the detection of the nucleus, or galaxies with photometry that may be contaminated by bright neighboring sources. After this procedure, we are left with 1655 X-ray sources that are spatially offset from their candidate host-galaxy centroid.

### 2.5. X-Ray Spectral Modeling and Application of Luminosity Thresholds

We convert the observed CSC2 0.5−7 keV aperture fluxes to unabsorbed, rest-frame 0.5−7 keV fluxes assuming an intrinsic model for the accreting source. Based on detailed spectral modeling of nearby ULXs (e.g., Swartz et al. 2004; Winter et al. 2006; Gladstone et al. 2009; Sutton et al. 2013; Walton et al. 2018), the X-ray emission is often successfully described by a combination of a blackbody component and a power-law component. While most CSC2 sources do not have sufficient counts for multicomponent spectral models, power-law and blackbody models are provided by the CSC2[9] for sources with >150 counts in the 0.5−7 keV energy range. In these cases, the power-law models generally provide a superior fit over the blackbody models based on the reduced statistic. Therefore, we assume power-law components ($S \sim E^{-\Gamma}$) to describe the accreting sources.

In our models, we attenuate these power-law components by photoelectric absorption in the Milky Way along the line of sight ($n_{\rm H,Gal}$; estimated from the `colden` function within `CIAO`) and by absorption intrinsic to the host galaxy ($n_{\rm H,exgal}$). If the CSC2 provides a power-law spectral index ($\Gamma_{\rm CSC}$) and a column density ($n_{\rm H,CSC}$) for a source, then we set $\Gamma = \Gamma_{\rm CSC}$ and $n_{\rm H,exgal} = n_{\rm H,CSC} - n_{\rm H,Gal}$. Otherwise, we fix the spectral index at $\Gamma = 2.1$ and the intrinsic absorption to $n_{\rm H,exgal} = 3 \times 10^{21}$ cm$^{-2}$ (see, e.g., Walton et al. 2022, and references therein). Unabsorbed, rest-frame X-ray luminosities ($L_{0.5-7,\rm unabs}$) are computed using the host-galaxy redshifts (Section 2.1) and cosmology stated in Section 1.

To select X-ray sources that are consistent with the traditional definition of ULXs, we impose a lower-luminosity limit of $L_{0.5-7,\rm unabs} = 10^{39}$ erg s$^{-1}$ (the conventional lower threshold for ULX selection corresponding to the approximate theoretical Eddington limit for a $10\,M_{\odot}$ BH). To avoid AGN and likely IMBH candidates (e.g., ESO 243-49 HLX-1; Farrell et al. 2009), we also impose an upper X-ray luminosity limit of $2 \times 10^{41}$ erg s$^{-1}$. This limit is motivated by the currently most-luminous known ULX that is confirmed to be associated with accretion onto a stellar-mass object (Israel et al. 2017a; converted to $L_{0.5-7,\rm unabs}$ from the peak 0.3–10 keV luminosity assuming a power-law spectrum with a photon index of $\Gamma = 2.1$). As in Walton et al. (2011) and Earnshaw et al. (2019), to retain the largest sample of ULX candidates, we also include sources that are consistent with these lower and upper luminosity thresholds when accounting for their upper and lower uncertainties, respectively. These limits yield 273 spatially offset X-ray sources that satisfy the luminosity criteria for ULXs.

[9] https://cxc.cfa.harvard.edu/csc/columns/spectral_properties.html

**Table 1**
ULX Candidates

| CSC2 Source | SDSS Host Galaxy | $z$ | Offset | $L_{0.5-7\ \mathrm{keV}}$ | $M_\star$ | SFR |
|---|---|---|---|---|---|---|
| (−) | (−) | (−) | (kpc) | ($10^{39}$ erg s$^{-1}$) | ($\log(M_\star/M_\odot)$) | ($\log(\mathrm{SFR}/M_\odot\ \mathrm{yr}^{-1})$) |
| 1 | 2 | 3 | 4 | 5 | 6 | 7 |
| 2CXO J000120.2+130641 | J000119.98+130640.59 | 0.018[a] | $1.39 \pm 0.20$ | $4.9^{+1.5}_{-1.5}$ | $12.0 \pm 0.41$ | $-3.6 \pm 3.80$ |
| 2CXO J000131.2+233409 | J000131.33+233403.97 | 0.070[a] | $7.99 \pm 1.94$ | $98.0^{+30.3}_{-30.3}$ | $9.7 \pm 1.17$ | $0.3 \pm 0.56$ |
| 2CXO J000846.5+192147 | J000846.76+192146.84 | 0.138[a] | $6.95 \pm 1.58$ | $144.0^{+123.5}_{-123.4}$ | $9.7 \pm 1.09$ | $0.1 \pm 0.37$ |
| 2CXO J001335.6−192804 | J001335.55−192805.75 | 0.148[a] | $7.76 \pm 2.05$ | $26.8^{+22.9}_{-23.9}$ | $11.2 \pm 0.09$ | $1.5 \pm 0.01$ |
| 2CXO J002231.2+002110 | J002231.07+002109.59 | 0.04715[b] | $2.24 \pm 0.71$ | $6.0^{+2.6}_{-2.6}$ | $8.8 \pm 0.03$ | $-2.7 \pm 0.01$ |
| 2CXO J003413.6−212803 | J003414.03−212811.00 | 0.02329[b] | $4.51 \pm 0.40$ | $6.7^{+3.3}_{-3.5}$ | $10.5 \pm 0.09$ | $0.8 \pm 0.01$ |
| 2CXO J004852.6+315735 | J004852.84+315731.08 | 0.017[a] | $1.68 \pm 0.21$ | $0.7^{+0.3}_{-0.3}$ | $9.8 \pm 0.38$ | $1.5 \pm 0.08$ |
| 2CXO J004947.9+321632 | J004947.81+321639.80 | 0.01555[b] | $2.21 \pm 0.28$ | $1.7^{+0.5}_{-0.5}$ | $11.5 \pm 0.48$ | $1.0 \pm 0.48$ |
| 2CXO J005513.9+352600 | J005513.99+352603.00 | 0.03683[b] | $2.27 \pm 0.46$ | $4.5^{+2.4}_{-2.4}$ | $10.4 \pm 0.16$ | $1.1 \pm 0.60$ |
| 2CXO J011505.5+002546 | J011505.90+002546.84 | 0.030[b] | $2.88 \pm 0.82$ | $16.2^{+7.7}_{-7.7}$ | $8.5 \pm 0.22$ | $0.0 \pm 0.09$ |

**Notes.** Column 1: ULX candidate CSC2 source; column 2: ULX candidate host galaxy; column 3: best available redshift of the host galaxy in column 2; column 4: ULX candidate projected physical offset from the host-galaxy centroid; column 5: ULX candidate unabsorbed, rest-frame 0.5–7 keV luminosity; columns 6–7: ULX candidate host-galaxy stellar mass ($M_\star$) and star formation rate (SFR).
[a] Photometric redshift.
[b] Spectroscopic redshift.

(This table is available in its entirety in machine-readable form.)

### 2.6. Removing AGNs and Known Contaminants

We remove ULX candidates that are likely to be AGNs (i.e., accreting massive BHs) based on their mid-infrared (MIR) colors by crossmatching them with the Wide-field Infrared Survey Explorer (WISE; Wright et al. 2010) using a radius equal to five times the X-ray source positional uncertainty. After applying the 90% completeness criterion defined in Assef et al. (2018), we then identify and remove eight MIR AGN (this filter may miss some low-luminosity AGNs; e.g., Hickox et al. 2009; Barrows et al. 2021). We also remove four X-ray sources that have stellar counterparts in the Panoramic Survey Telescope and Rapid Response System (Pan-STARRS) $i$-band imaging (determined by applying models composed of Sérsic components and a background following the procedure in Barrows et al. 2019) because they may actually be associated with a distinct galaxy and hence are likely AGNs. Any possible remaining AGNs will have large X-ray-to-optical ratios or be in remnant stellar cores that have undergone significant tidal stripping (this scenario is more likely for IMBHs; see Section 1).

We also crossmatch the ULX candidates with NED (using the same crossmatch radius of five times the X-ray source positional uncertainty) to search for any association with known extended radio jets or gravitationally lensed AGNs because they can mimic offset X-ray sources; none are found. Using the same NED crossmatch, we identify and remove one ULX candidate that is coincident with a source possessing a spectroscopic redshift ($z = 0.53$) that is significantly different from that of its candidate host galaxy ($z = 0.01$).

As noted in Earnshaw et al. (2019) and Walton et al. (2022), host-galaxy AGNs may contaminate ULX samples if they are not coincident with the optical centroid of the host galaxy. Therefore, we follow the approach taken in those works to quantify the spatial offsets of X-ray AGNs. Of the subset of matches between X-ray sources and galaxies (Section 2.3), we identify X-ray AGNs as sources with unabsorbed, rest-frame 2–10 keV luminosities ($L_{2-10\ \mathrm{keV}}$) of $L_{2-10\ \mathrm{keV}} \geqslant 10^{42}$ erg s$^{-1}$ (converted from the observed 0.5–7 keV flux using the same procedure as described in Section 2.5, assuming a power-law spectrum and a typical AGN photon index of $\Gamma = 1.7$; e.g., Middleton et al. 2008). We then determine the relative uncertainties on the X-ray source offsets (as in Section 2.4). The X-ray AGN offsets are found to be smaller than the $3\sigma$ uncertainties in all cases, indicating that our statistical threshold is sufficient to exclude nuclear AGNs.

Finally, as noted in Walton et al. (2022), off-axis observations can bias the CSC2 fluxes toward high values due to large PSFs (and hence large extraction radii) that may incorporate emission from other sources in crowded fields or extended emission. Therefore, we visually inspect the extraction radii of each observation that contributes to the aperture flux for a master source (i.e., all OBSIDs in the best Bayesian block) and remove any sources for which the extraction regions incorporate clearly unrelated sources or extended emission. One source is flagged and removed in this step.

### 2.7. Final Sample

The final sample contains 259 unique ULX candidates among 237 host galaxies. The ULX candidates, host galaxies, redshifts, projected physical offsets, and intrinsic 0.5−7 keV luminosities are listed in Table 1. While ULX candidates hosted by low-redshift galaxies have been extensively cataloged (Colbert & Ptak 2002; Swartz et al. 2004; Liu & Mirabel 2005; Liu & Bregman 2005; Liu 2011; Swartz et al. 2011; Gong et al. 2016; Earnshaw et al. 2019; Kovlakas et al. 2020; Inoue et al. 2021; Walton et al. 2022), few are known out to intermediate redshifts. This sample increases the known number of ULX candidates past $z \sim 0.15$ by a factor of $\sim$3 and significantly past $z \sim 0.3$ for the first time.

The redshift distribution is shown along the top axis of Figure 3 and spans the range $z = 0.002$–$0.51$, where 77% (200) have spectroscopic redshifts, and the remaining 23% (59) have only photometric redshifts. The majority of spectroscopic redshifts obtained from the literature (i.e., not from the SDSS) are for relatively nearby galaxies, leading to the observed bias of spectroscopic redshifts toward lower values compared to

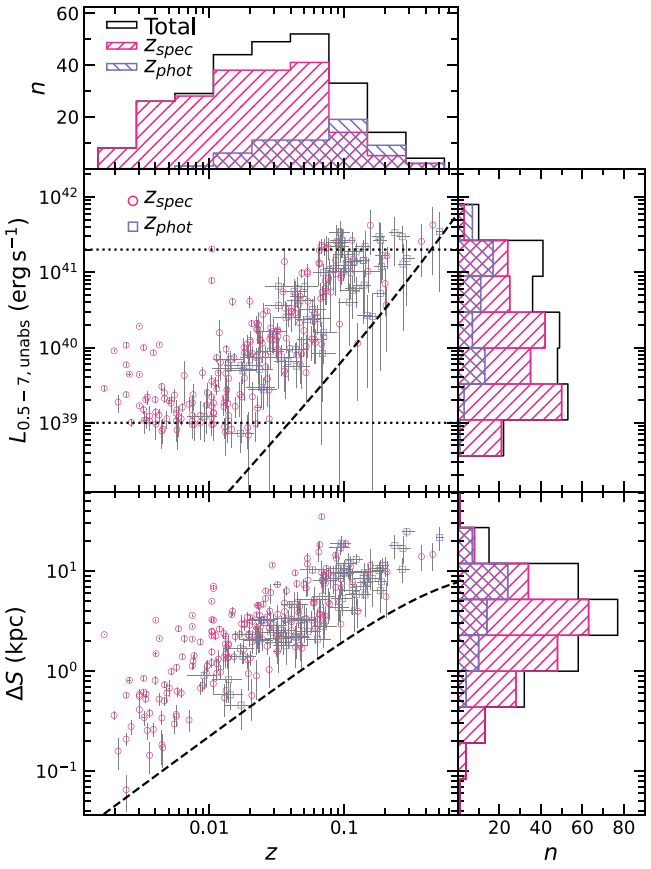


**Figure 3.** Unabsorbed, rest-frame 0.5–7 keV luminosity ($L_{0.5-7,\mathrm{unabs}}$; top) and projected physical offset from the host-galaxy centroid ($\Delta S$; bottom) against redshift ($z$) for our final sample of ULX candidates (Section 2.7). The samples with and without spectroscopic redshifts are indicated by the magenta circles and purple squares, respectively. The positive correlations of both $L_{0.5-7,\mathrm{unabs}}$ and $\Delta S$ with $z$ result in redshift-dependent selection biases toward luminous ULX candidates with large physical offsets at high redshifts. The dashed lines represent the minimum 0.5–7 keV flux sensitivity (top) and the minimum resolvable physical offset (bottom) from the final sample. The dotted lines denote the lower and upper luminosity thresholds for ULX selection (Section 2.5).

photometric redshifts. The low-redshift limit of the sample reflects the distribution of nearby SDSS galaxies. Due to the CSC2 sensitivity limits, a redshift-dependent luminosity bias exists (upper plot of Figure 3). Moreover, due to the angular resolution limits imposed by the Chandra PSF (Section 2.2) and the relative astrometric accuracy (Section 2.4), a redshift-dependent physical offset bias also exists (lower plot of Figure 3).

Studies of nearby ULXs often reveal several candidates within a host galaxy (i.e., a mean of $\sim 2$; Ptak & Colbert 2004; Swartz et al. 2004; Liu & Mirabel 2005; Swartz et al. 2011; Earnshaw et al. 2019; Walton et al. 2022). When limiting our sample to a similar volume ($z < 0.05$), the mean number of ULX candidates per host galaxy (1.1) is lower by comparison (Figure 4), potentially due to systematic differences in the measured sizes of host-galaxy extents, to different criteria used for the X-ray source selection or a combination thereof. Figure 5 shows examples of host galaxies with multiple ULX candidates. More distant hosts typically contain only one identified ULX candidate due to X-ray imaging sensitivity limits and to the PSFs that limit the selection of off-nuclear sources (Hornschemeier et al. 2004; Lehmer et al. 2006; Mainieri et al. 2010). We similarly observe a declining number

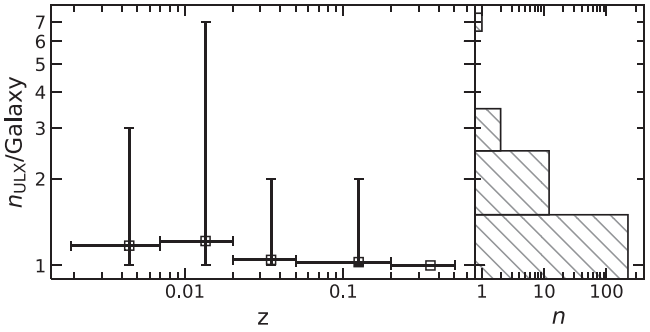


**Figure 4.** Number of ULX candidates in each host galaxy ($n_{\mathrm{ULX}}$/galaxy) against the host-galaxy redshift ($z$). Data points represent mean values in redshift bins that are approximately even in logarithmic space and adjusted to have a minimum of 15 ULX candidates per bin: $z = 0.002$–$0.007$, $0.007$–$0.02$, $0.02$–$0.05$, $0.05$–$0.2$, and $0.2$–$0.51$. Vertical error bars represent the full range of values in each bin, and horizontal error bars denote the bin width. The distribution of $n_{\mathrm{ULX}}$ is shown on the right. $n_{\mathrm{ULX}}$ decreases with redshift due to the decreasing angular size of the host galaxies and the CSC2 sensitivity limits.

of ULX candidates per host galaxy with increasing redshift (Figure 4). Examples of host galaxies with only one ULX candidate, extending out to the maximum redshift of our sample, are shown in Figure 6.

Additional quality flags are available for master sources in the CSC2 (`likelihood_class`, `sat_src_flag`, `dither_warning_flag`, `streak_src_flag`, and `pileup_flag`), some of which have been incorporated by previous catalogs of nearby ULX candidates from the CSC2 (Kovlakas et al. 2020; Walton et al. 2022). Among our final sample, 60 (24%) have a `likelihood_class` value of `MARGINAL`, while the remaining 199 (76%) have a value of `TRUE`. Only one source has a `dither_warning_flag` set, and none of the other flags are set. Because detections near the flux sensitivity limits will more often be `MARGINAL`, we include both types in our sample to probe higher redshifts. Our subsequent qualitative conclusions regarding contamination fractions (Section 3), host-galaxy properties (Section 4), comparison with XRBs (Section 5), and occupation fractions (Section 6) remain unchanged when the sample is limited to sources with `likelihood_class = TRUE` and with no other flags. However, in Section 7 we discuss the impact of these flags on our results regarding the ULX contribution to the CXB.

### 2.8. Diffuse Emission and Source Confusion

We compute the 0.5−7 keV emission expected from hot ISM gas using the host-galaxy SFRs (Section 4), the 0.3−10 keV relation from Mineo et al. (2012), and a thermal power-law index of $\Gamma = 3$ (e.g., Mezcua et al. 2016; Barrows et al. 2019). We then scale this value by the ratio of the Chandra PSF area to the total galaxy area (subtended by the Petrosian radius). In Sections 5.2 and 7 we remove this estimated hot gas contribution when examining how the ULX candidate luminosities and fluxes evolve with redshift.

A single CSC2 detection may represent multiple physically distinct X-ray sources that are unresolved by Chandra, particularly at higher redshifts. To test this effect on our results, for each ULX candidate we compute the value of $L_{0.5-7,\mathrm{unabs}}$ that would be detected assuming the host galaxy has the same X-ray point-source population as the Antennae galaxy system (a merger between NGC 4038 and NGC 4039 and a prototypical XRB/ULX-rich system due to the recent

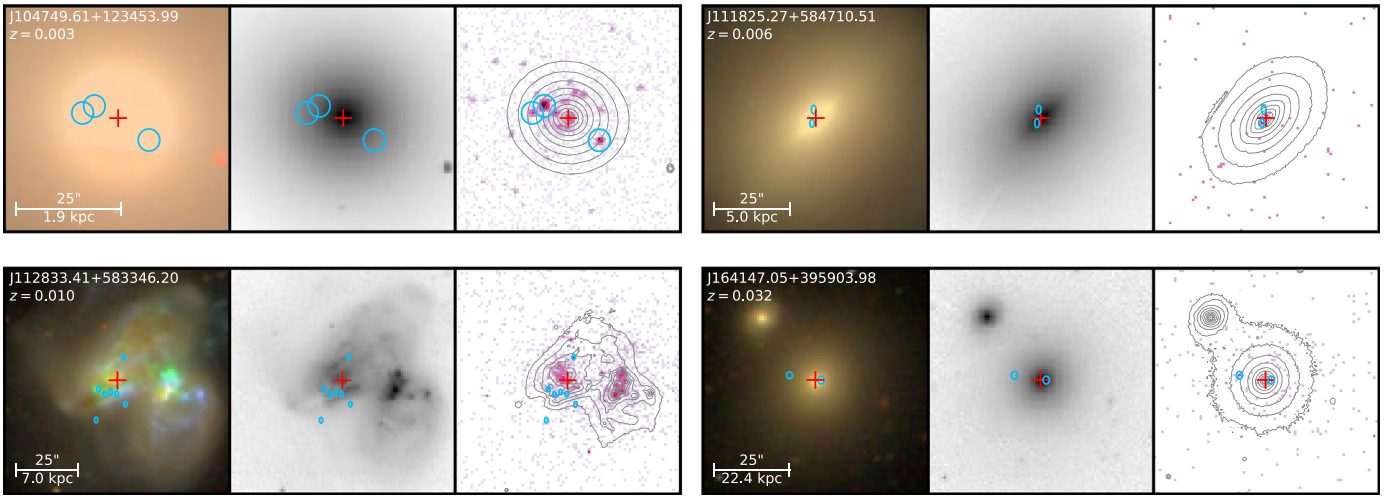


**Figure 5.** Host galaxies with multiple ULX candidates. Left: SDSS $g + r + i$ color composite image; middle: Pan-STARRS $i$-band image; right: Chandra 0.5–7 keV rest-frame image with the Pan-STARRS $i$-band image contours overlaid. The galaxy centroid is marked by a red cross and the ULX candidate positions and errors are indicated with blue ellipses. The examples represent host galaxies with the maximum number of ULX candidates in redshift bins of approximately even logarithmic spacing over the interval $z = 0.002$–$0.06$ and defined by the following boundaries: $z = [0.002, 0.005, 0.01, 0.03, 0.06]$.

merger-triggered star formation; e.g., Fabbiano et al. 2001; Zezas et al. 2006). We use the list of Antennae X-ray sources from Poutanen et al. (2013) and convert the 0.1−10 keV luminosities to $L_{0.5-7,\mathrm{unabs}}$ using the best-fit power-law spectral indices from Zezas et al. 2002. For each ULX candidate, we determine the total emission from X-ray sources in the Antennae (placed at the host-galaxy redshift) that would be confused due to the CSC2 PSF ($L_{0.5-7,\mathrm{Conf}}$). To account for spatial variations of the Antennae X-ray point-source population, we compute $L_{0.5-7,\mathrm{Conf}}$ centered at 1000 random positions within the Antennae light profile (as defined in Poutanen et al. 2013).

The maximum number of confused X-ray point sources from these estimates reaches 11 at the highest redshifts of our sample due to the significant physical extents of the Chandra PSF profiles. This suggests that the luminosities of some of our ULX candidates may be due to the integrated emission of several ULXs plus diffuse emission from hot ISM gas. In Section 6 we use these results to correct the ULX occupation fraction estimates for source confusion.

## 3. Contamination Fractions

While known contaminants are removed in Section 2.6, here we estimate the number of unknown background or foreground sources that remain. Following the methodology applied to previous nearby ULX catalogs (Walton et al. 2011; Sutton et al. 2012; Earnshaw et al. 2019; Walton et al. 2022), we compute the number of X-ray sources expected to randomly be within the area of each galaxy in the parent sample (a circle defined by the Petrosian radius) minus the inner offset threshold rectangle (defined by three times the offset uncertainty in R.A. and decl.). The parent galaxy offset uncertainties are the quadrature sum of the relative astrometric uncertainty between the SDSS image and the overlapping Chandra images (computed as described in Section 2.4) and the average CSC2 source centroid error from our final sample.

We determine the expected number of X-ray sources using the resolved 0.5–7 keV point-source density function of Masini et al. (2020) and the effective limiting sensitivities at each galaxy position. We set the effective limiting sensitivity to the flux corresponding to an observed 0.5–7 keV luminosity of $10^{39}$ erg s$^{-1}$ at the host-galaxy redshift, or otherwise the 0.5–7 keV CSC2 limiting sensitivity at the galaxy position if it is larger (where the CSC2 limiting sensitivities are obtained from the CSC2 all-sky limiting sensitivity map that corresponds to the deepest sensitivity value among all stacks that cover a given position[10]). We omit any parent galaxies with CSC2 limiting sensitivities corresponding to greater than the maximum luminosity of our selection ($L_{0.5-7,\mathrm{unabs}} = 2 \times 10^{41}$ erg s$^{-1}$). The contamination fraction is then the total number of expected X-ray sources in the parent sample divided by the total number of ULX candidates (with the AGN identified in Section 2.6 removed from both quantities).

Figure 7 shows how the expected fraction of contaminants varies with redshift. The fractions for the full sample and the subset with `likelihood_class` values of TRUE and without any quality flags set (see Section 2.7) are consistent when accounting for the uncertainties. Moreover, our estimates are statistically consistent with those from previous samples at both low and intermediate redshifts. The overall mean contamination fraction is $31\% \pm 4\%$, and no statistically significant evidence for redshift evolution is detected.

## 4. Host-galaxy Properties

Stellar masses ($M_\star$) and SFRs for each host galaxy are computed by applying models to broadband spectral energy distributions (SEDs) using the Code Investigating GALaxy Emission (`CIGALE`; Noll et al. 2009; Boquien et al. 2019) that accounts for absorbed and reradiated starlight through an energy balance approach. To build the SEDs, we supplement the SDSS photometry with detections from the Galaxy Evolution Explorer (GALEX; Bianchi & GALEX Team 1999), the Two Micron All Sky Survey (2MASS; Skrutskie et al. 2006), and WISE (using a matching radius of 2″). Our models assume a delayed star formation history, a Salpeter initial mass function (Salpeter 1955), and the stellar population libraries of Bruzual & Charlot (2003). Lower and upper bounds on the best-fit parameters are the 16th and 84th percentiles determined

[10] https://cxc.cfa.harvard.edu/csc/char.html

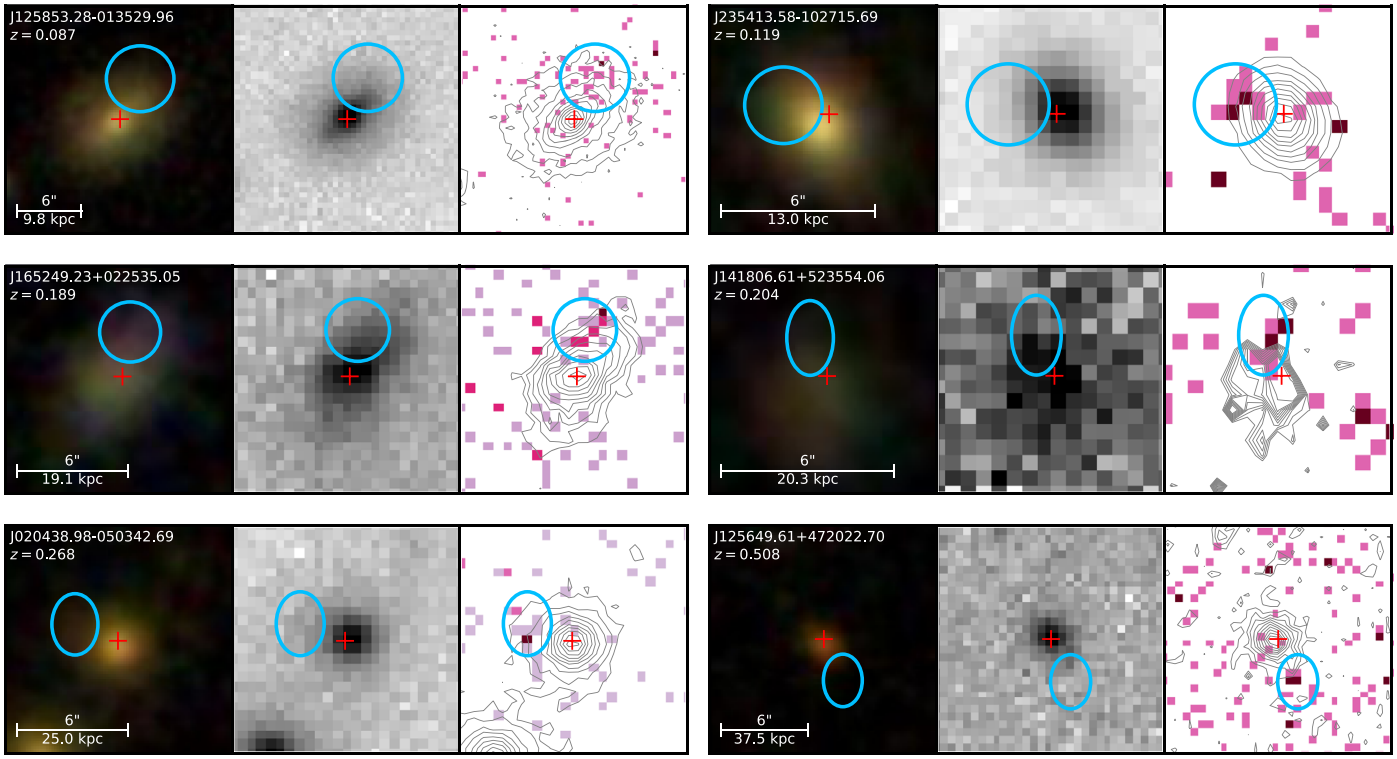


**Figure 6.** Same as Figure 5 but for host galaxies over the redshift range not sampled by galaxies with more than one ULX. The examples represent ULX candidates with the median $L_{0.5-7,\mathrm{unabs}}$ value in redshift bins of approximately even logarithmic spacing over the interval $z = 0.06$–$0.52$ and defined by the following boundaries: $z = [0.06, 0.1, 0.15, 0.20, 0.25, 0.35, 0.52]$.

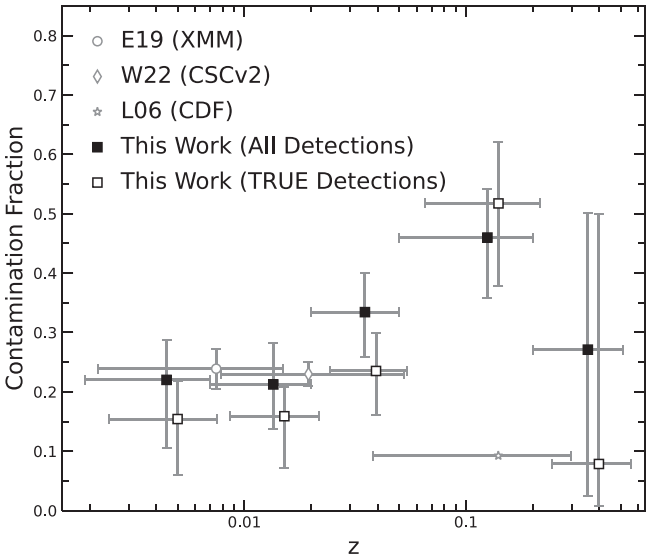


**Figure 7.** Contamination fraction against redshift ($z$) for our full sample of ULX candidates (filled squares) and the subset with `likelihood_class` values of TRUE and without any quality flags set (open squares, horizontally offset for clarity). The redshift bins are defined in Figure 4. Vertical error bars represent the upper and lower 68.3% binomial confidence intervals, and horizontal error bars represent the bin width. We also show comparison estimates from a Chandra Deep Field sample (Lehmer et al. 2006; L06), an XMM-Newton sample (Earnshaw et al. 2019; E19), and a CSC2 sample (Walton et al. 2022; W22), plotted at the sample mean or median distances and with uncertainties shown (if published). When accounting for uncertainties, our estimates are consistent with those from previous catalogs of both nearby and intermediate-redshift ULX candidates.

from fits to synthetic data created from random Gaussian distributions with standard deviations equal to the photometry uncertainties.

We run additional models that also include an AGN component, and an AGN is considered to be present if the F-distribution probability is greater than 90%. This corresponds to six galaxies, none of which show evidence for a nuclear X-ray source. Hence, their ULX candidates may instead be massive BHs with AGN-like SEDs. Alternatively, a heavily obscured AGN (undetected in X-rays) may be present, or an AGN component is simply inaccurately included in the SED model due to poor photometry or fitting results.

The values of $M_\star$ and SFR for the ULX candidate host galaxies are listed in Table 1. The SFR is plotted against $M_\star$ in Figure 8, and (when accounting for uncertainties) both the parent and ULX candidate hosts are in agreement with expectations from normal star-forming galaxies. The ULX candidate hosts show a systematic offset toward larger specific SFRs (sSFRs), where the median offset is $\Delta\mathrm{sSFR} = 0.48$ dex. While the statistical significance of the offset is weak in each stellar-mass bin, the trend is consistent with observed preferences for ULXs to be found in galaxies with relatively high SFRs (e.g., Swartz et al. 2009).

## 5. Comparison to XRB Populations

Several studies of local ULXs have identified their optical counterparts to be massive stars (e.g., Motch et al. 2014; Heida et al. 2015, 2019), suggesting that ULXs may be preferentially associated with HMXBs. Indeed, the results from Section 4 and Figure 8 show that the ULX candidate hosts exhibit a systematic offset toward large sSFRs (relative to the parent galaxy sample) that is expected if HMXBs dominate the sample. However, as suggested by the presence of ULXs in early-type galaxies (e.g., Plotkin et al. 2014), in some cases they may instead be associated with LMXBs.

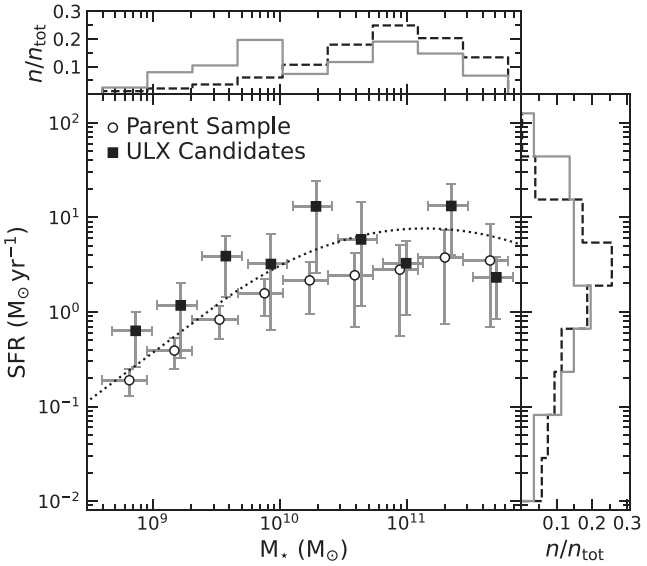


**Figure 8.** Galaxy SFR against stellar mass ($M_\star$). The dotted line shows the redshift-dependent relation from Schreiber et al. (2015), computed using the median redshift of the parent galaxy sample. The data points represent the median SFRs of the parent galaxy sample (open circles) and ULX candidate hosts (filled squares) in bins of even logarithmic spacing along the abscissa (horizontally offset for clarity). The vertical error bars represent the two-sided standard deviation within the bin, and the horizontal error bars denote the bin width. Histograms for values along the ordinate and abscissa (each normalized to unity) are shown on the right and top, respectively, for the parent sample (black dashed) and ULX candidate hosts (gray solid). Both samples are generally consistent with the relation for star-forming galaxies, though the specific SFRs of ULX candidate hosts are systematically elevated relative to those of the parent sample.

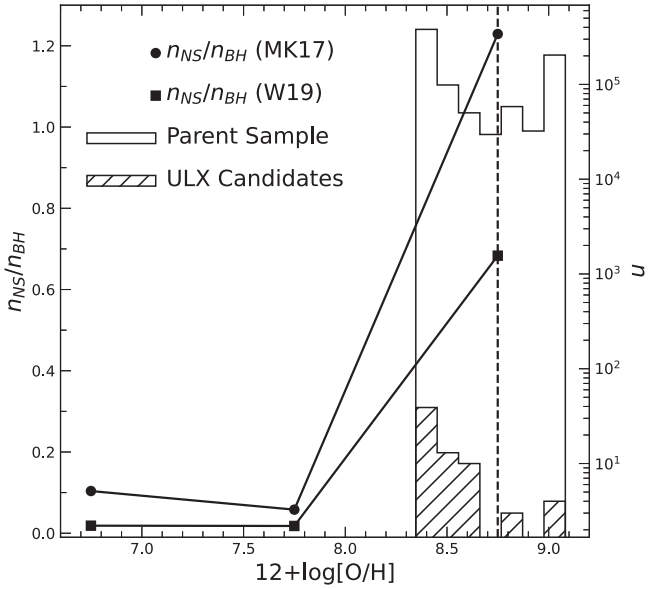


**Figure 9.** Left ordinate: predicted ratio of neutron star to BH accretors ($n_{\rm NS}/n_{\rm BH}$) as a function of host-galaxy metallicity (O/H) from the population synthesis models of Middleton & King (2017) (MK17; filled circles) and Wiktorowicz et al. (2019) (W19; filled squares). Right ordinate: number ($n$) of galaxies in our parent sample (open histogram) and in the sample of ULX candidate hosts (hatched histogram). Metallicity estimates are derived from fitted stellar population models (Section 5.1) that consist of seven different values: $\log[{\rm O/H}]+12 = 8.35$, 8.45, 8.55, 8.65, 8.75, 8.85, and 8.95. The vertical dashed line indicates solar metallicity. The ULX host galaxies show a preference for low metallicities relative to the parent sample, and they are mostly consistent with subsolar metallicities. The predicted $n_{\rm NS}/n_{\rm BH}$ ratios suggest at least some contribution from BH accretors.

Because the spatial resolution of our host-galaxy imaging precludes the identification of stellar counterparts, to constrain the nature of our ULX candidates, we instead compare their global host-galaxy properties with those of XRBs. In Section 5.1 we examine their host-galaxy metallicities, and in Section 5.2 we determine how their X-ray powers scale with their host-galaxy stellar masses and SFRs.

### 5.1. Host-galaxy Metallicities

Decreasing metallicities are observed to correlate with increasing numbers of ULXs per host galaxy (e.g., Zampieri & Roberts 2009; Mapelli et al. 2010; Prestwich et al. 2013; Douna et al. 2015; Kovlakas et al. 2020), consistent with a significant contribution from HMXBs. Theoretical results also predict that metallicity plays a strong role in the type of accretors found in ULXs, with larger neutron star (versus BH) contributions for higher metallicities (e.g., Middleton & King 2017; Wiktorowicz et al. 2019).

For the subset of ULX candidate hosts in our sample that were spectroscopically selected as galaxies in the Baryon Oscillation Spectroscopic Survey (BOSS; Dawson et al. 2013), metallicity estimates are available from model grids (generated using Flexible Stellar Population Synthesis; Conroy et al. 2009) fitted to the SDSS photometry (Montero-Dorta et al. 2016). When using the subset of these model results that allow for an extended star formation history and account for dust, the metallicities of our ULX candidate host galaxies show a bias toward low values relative to the parent sample (a two-sample Kolmogorov–Smirnov test yields a null hypothesis probability of $10^{-13}$ that they are identical) that suggests a preference for hosting HMXBs (Figure 9). This is also consistent with the observed over-abundances of ULX candidates in low-mass galaxies (and hence low-metallicity environments; e.g., Griffith et al. 2011; Rémy-Ruyer et al. 2015; O'Connor et al. 2016) reported in previous studies (e.g., Swartz et al. 2008; Kovlakas et al. 2020) and apparent in the top histogram of Figure 8 for our sample.

The host-galaxy metallicities are predominantly subsolar, consistent with samples of nearby HMXBs (e.g., Brorby et al. 2016; Fornasini et al. 2019, 2020; Lehmer et al. 2021). When compared to predictions from the population synthesis models of Middleton & King (2017) and Wiktorowicz et al. (2019), our results are generally consistent with contributions from both neutron star and BH accretors. These predictions vary negligibly over the redshift range of our sample.

### 5.2. Scaling Relations with Host-galaxy Stellar Mass and SFR

Because LMXB and HMXB X-ray emissivity scale with host-galaxy $M_\star$ and SFR, respectively, the sSFR provides a strong indicator of their relative X-ray contributions. The evolution of sSFR with $z$ is shown in the top panel of Figure 10, and the values are statistically consistent with similar contributions from both LMXBs and HMXBs ($\rm sSFR = 5.6 \times 10^{-11}$ yr$^{-1}$; Lehmer et al. 2010) over the full sample redshift range. However, a systematic offset toward a stronger HMXB contribution is observed (median value of $\rm sSFR = 1.3 \times 10^{-10}$ yr$^{-1}$).

The middle and bottom panels of Figure 10 show how our sample compares to the hard X-ray (2−10 keV) LMXB and HMXB galaxy scaling relations ($L_H/M_\star$ and $L_H/{\rm SFR}$, respectively) for local samples (Boroson et al. 2011; Mineo et al. 2012) and as a

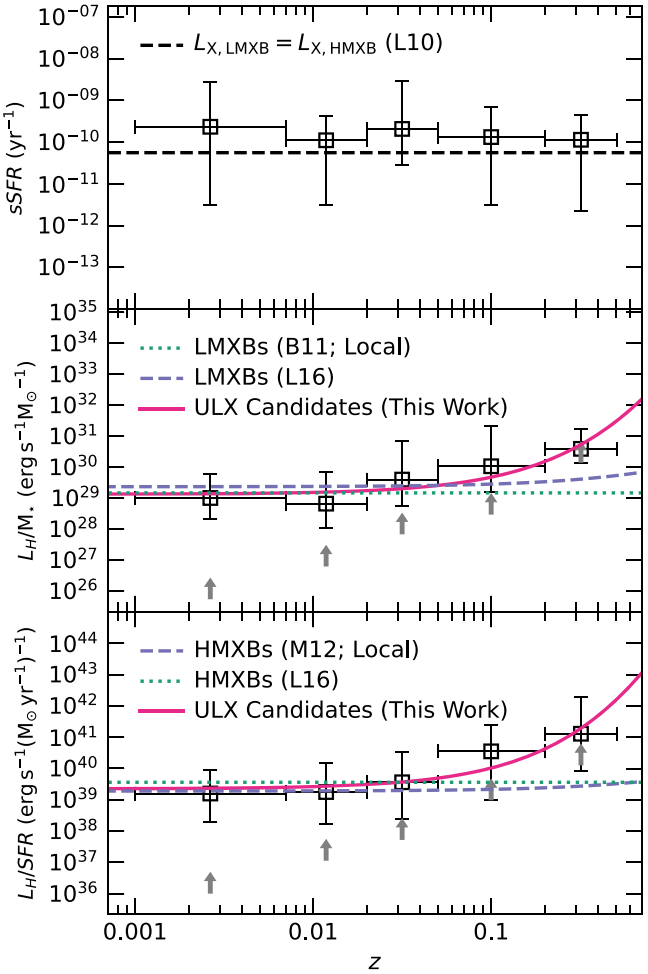


**Figure 10.** Top: specific SFR (sSFR) against redshift. The black dashed line denotes the value of sSFR above which HMXBs dominate the X-ray emission of their host galaxies, relative to LMXBs, from Lehmer et al. (2010) (L10). At each redshift, the sSFRs are consistent with similar contributions though they systematically deviate toward a larger HMXB contribution. Middle and bottom panels: hard X-ray (2−10) luminosity over host-galaxy stellar mass ($L_H/M_\star$) and SFR ($L_H$/SFR). The green dotted lines represent the local relations from Boroson et al. (2011) (B11; middle) and Mineo et al. (2012) (M12; bottom), the purple dashed lines represent the redshift-dependent relations from Lehmer et al. (2016) (L16), and the magenta solid lines represent the best-fit power-law functions to our sample. In all panels, the open black squares represent the median values from our sample within the same redshift bins defined in Figure 4, the vertical error bars denote the standard deviation within the bins, and the horizontal error bars denote the bin widths. The gray arrows denote the average lower limits for our sample in each bin. Due to the luminosity limits, the scaling relations for our ULX candidate sample evolve more quickly with redshift (compared to XRBs).

function of redshift (Lehmer et al. 2016): $L_H/M_\star = \alpha(1+z)^\gamma$ and $L_H/\mathrm{SFR} = \beta(1+z)^\delta$ (where $\alpha = 10^{29.37\pm0.15}$ erg s$^{-1}$ $M_\odot^{-1}$, $\beta = 10^{39.28\pm0.05}$ erg s$^{-1}$($M_\odot$ yr$^{-1}$)$^{-1}$, $\gamma = 2.03 \pm 0.60$, and $\delta = 1.31 \pm 0.13$). Hard X-ray luminosities for our sample are computed using the same spectral models described in Section 2.5, and they are corrected for the contribution from hot ISM gas (Section 2.8). When parameterized with the same power law functional form, our sample yields consistent normalizations of $\alpha = 10^{29.1^{+0.8}_{-2.1}}$ erg s$^{-1}$ $M_\odot^{-1}$ and $\beta = 10^{39.4^{+0.8}_{-1.8}}$ erg s$^{-1}$($M_\odot$ yr$^{-1}$)$^{-1}$ (offsets at the 0.3$\sigma$ and 0.1$\sigma$ levels, respectively). This agreement suggests that, for nearby host galaxies, ULX luminosities have a dependence on host stellar mass and SFR similar to that of typical XRB populations.

However, the fits to our sample yield significantly larger power-law slopes of $\gamma = 13.3^{+0.6}_{-0.9}$ and $\delta = 16.0^{+0.7}_{-0.6}$ (offsets at the 12$\sigma$ and 20$\sigma$ levels, respectively). As indicated by the lower limits shown in the middle and bottom panels of Figure 10, this stronger redshift evolution is likely reflecting that our sample is biased toward luminous X-ray sources at higher redshifts (e.g., the top panel of Figure 3) compared to the deeper stacks from Lehmer et al. (2016). Therefore, at higher redshifts, our procedure is selecting a subset of luminous LMXBs and HMXBs with highly efficient accretion rates. While the larger ratios of X-ray luminosity to stellar mass and SFR may possibly be elevated due to AGN contamination, an AGN component is not favored in the SED models (Section 4) of any host galaxies above $z = 0.15$ (where our sample significantly deviates from that of XRB populations). Moreover, any such AGN would not be MIR detected, nor would they have optical counterparts detected by the Pan-STARRS imaging (Section 2.6). Hence, if AGNs, they are likely powered by accretion onto IMBHs.

## 6. Redshift Evolution of the ULX Occupation Fraction

For galaxies in the nearby universe, Hornschemeier et al. (2004) estimate that the ULX occupation fraction (fraction of galaxies that host at least one ULX candidate) is $8^{+8}_{-5}$%, and Ptak & Colbert (2004) find a similar value of up to ∼10%−20%. On the other hand, at higher redshifts ($z = 0.03 - 0.25$) Hornschemeier et al. (2004) estimate a fraction of $36^{+24}_{-15}$% in the Chandra Deep Fields. Over a similar redshift range and with an augmented sample, Lehmer et al. (2006) estimate a fraction of up to ∼30%. Moreover, when compared to a matched local sample from Ptak & Colbert (2004), they find the intermediate-redshift ULX occupation fraction to be elevated at the 80% level. If ULXs are predominantly associated with HMXBs, their increasing galaxy occupation fractions with redshift may be explained by the increase in SFR comoving density with redshift due to higher cold gas fractions, lower metallicities, and merger-triggered star formation (e.g., Madau & Dickinson 2014 and references therein). Enhanced galaxy merger rates may also lead to the presence of off-nuclear accreting IMBHs with faint stellar cores that would contribute to the observed ULX fraction.

However, these results are based on comparisons between multiple different samples that introduce a heterogeneous set of selection biases. For instance, using an intermediate-redshift sample of ULX candidates from the COSMOS field, Mainieri et al. (2010) find a ULX occupation fraction that is several times to an order of magnitude lower than that from the Chandra Deep Field samples, potentially due to shallower flux limits that inhibit detection of the lowest luminosity ULXs. Therefore, we use our sample of uniformly-selected ULXs over the range $z = 0.002-0.51$ to estimate the redshift evolution of the ULX occupation fraction in a consistent manner and out to $z \sim 0.5$ for the first time.

Following the procedures from Ptak & Colbert (2004) and Lehmer et al. (2006), in logarithmically spaced luminosity bins over the range $10^{39}-2\times10^{41}$ erg s$^{-1}$, we first determine the number of parent sample galaxies with limiting 0.5−7 keV luminosities (see Section 3) greater than or equal to the bin lower edge. In each bin, the ULX occupation fraction is the number of those galaxies with a ULX of observed 0.5−7 keV luminosity equal to or greater than the bin lower limit divided by the total number of galaxies (we are using observed

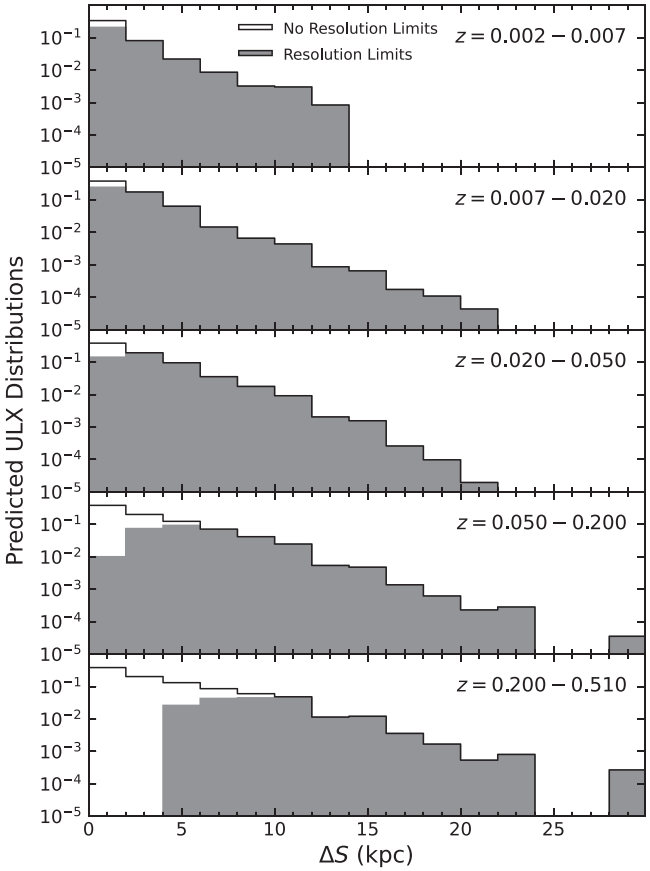


**Figure 11.** Predicted number of ULXs in our sample (normalized to a sum of unity) that could be found in our sample, with (solid gray) and without (open) the resolution limits imposed, as a function of projected physical separation ($\Delta S$) and in the same redshift bins defined in Figure 4. The fraction of recovered ULXs is the ratio of the two distributions, and it declines with increasing redshift. The larger physical offsets observed at higher redshifts are a result of the bias illustrated in the lower panel of Figure 3.

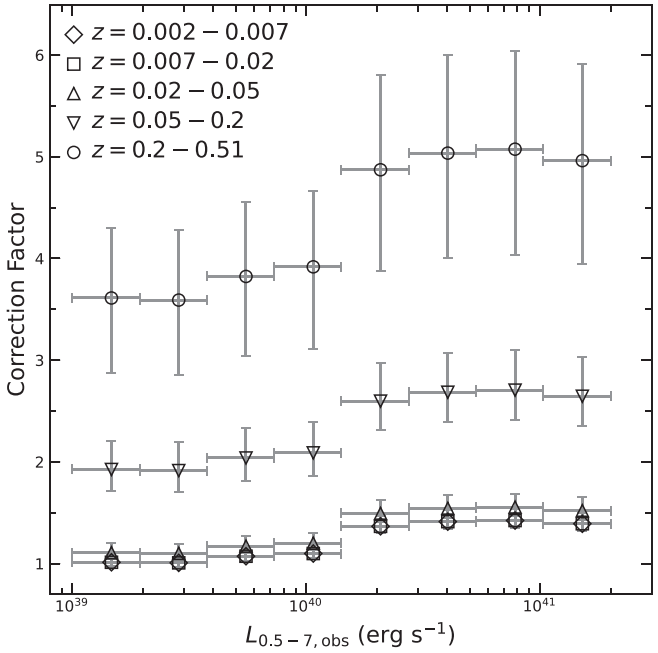


**Figure 12.** Spatial resolution correction factor for the observed ULX occupation fractions, computed as a function of observed 0.5−7 keV luminosity ($L_{0.5-7,\mathrm{obs}}$) and in the five redshift bins defined in Figure 4. The vertical error bars denote the 68.3% binomial confidence intervals, and the horizontal error bars denote the bin widths.

luminosity, rather than unabsorbed, rest-frame luminosity because that is directly comparable to the limiting luminosity).

The Chandra angular resolution introduces a bias that misses ULXs with small projected physical offsets at high redshifts (i.e., the lower panel of Figure 3). To correct for this bias, we follow the procedure from Lehmer et al. (2006) that consists of estimating the number of our ULX candidate host galaxies for which an offset X-ray source could be detected, both with and without imposing the resolution limits (i.e., the offset uncertainties) as a function of projected physical separation. We then convolve both of these distributions with the normalized true distribution of ULXs (taken from Kovlakas et al. 2020 and restricted to a distance of <40 Mpc and nuclear offsets of >0.05 kpc for a complete sample not limited by spatial resolution) to obtain the predicted true distributions for our sample. Because the resolution limits have a greater impact on the detectable physical offsets at higher redshifts, we compute these distributions as a function of redshift (Figure 11). The ratio of these distributions yields the spatial resolution correction factor as a function of redshift. As in Lehmer et al. (2006), we also correct for the different numbers of ULXs per galaxy between our sample and that of Kovlakas et al. (2020) as a function of observed luminosity. The final spatial resolution correction factors are shown in Figure 12.

After correcting for spatial resolution limits, in addition to contamination (Section 3) and galaxy inclination (Section 2.3), the ULX occupation fractions are shown in the left panel of Figure 13. Our estimated fractions decrease with increasing luminosity, consistent with the negative correlations observed both locally (Ptak & Colbert 2004) and at intermediate redshifts (Lehmer et al. 2006; Mainieri et al. 2010). The redshift-dependent luminosity bias imposed by the CSC2 sensitivity limits (i.e., the top panel of Figure 3) is reflected in the trend of increasing median ULX candidate redshift with luminosity and in the absence of lower-luminosity sources at higher redshifts.

Source confusion is discussed in Section 2.8 using the Antennae merging galaxy system as a template, and here we use those results to correct for this effect. We first subtract the expected hot ISM gas contribution from each ULX candidate. Assuming the remaining emission is a superposition of luminosities from multiple X-ray sources and that this number is equal to the median number of confused Antennae X-ray point sources, we divide it by this number to obtain the corrected luminosities of the sources contributing to the observed emission (assuming the observed emission is distributed equally among the confused sources). Then, the luminosities of each bin are adjusted based on the mean correction factor in each bin. The corrected luminosities of the occupation fractions are shown in the right panel of Figure 13, with the corrections being strongest at higher redshifts. The horizontal error bars include the range of values obtained when assuming the minimum and maximum estimated numbers of confused sources to convey the uncertainties associated with these corrections.

For a given X-ray luminosity, the ULX occupation fractions increase with redshift, even after correcting for confusion. This trend is qualitatively consistent with that inferred from comparisons of local and intermediate-redshift samples (Hornschemeier et al. 2004; Lehmer et al. 2006; Mainieri et al. 2010) despite the

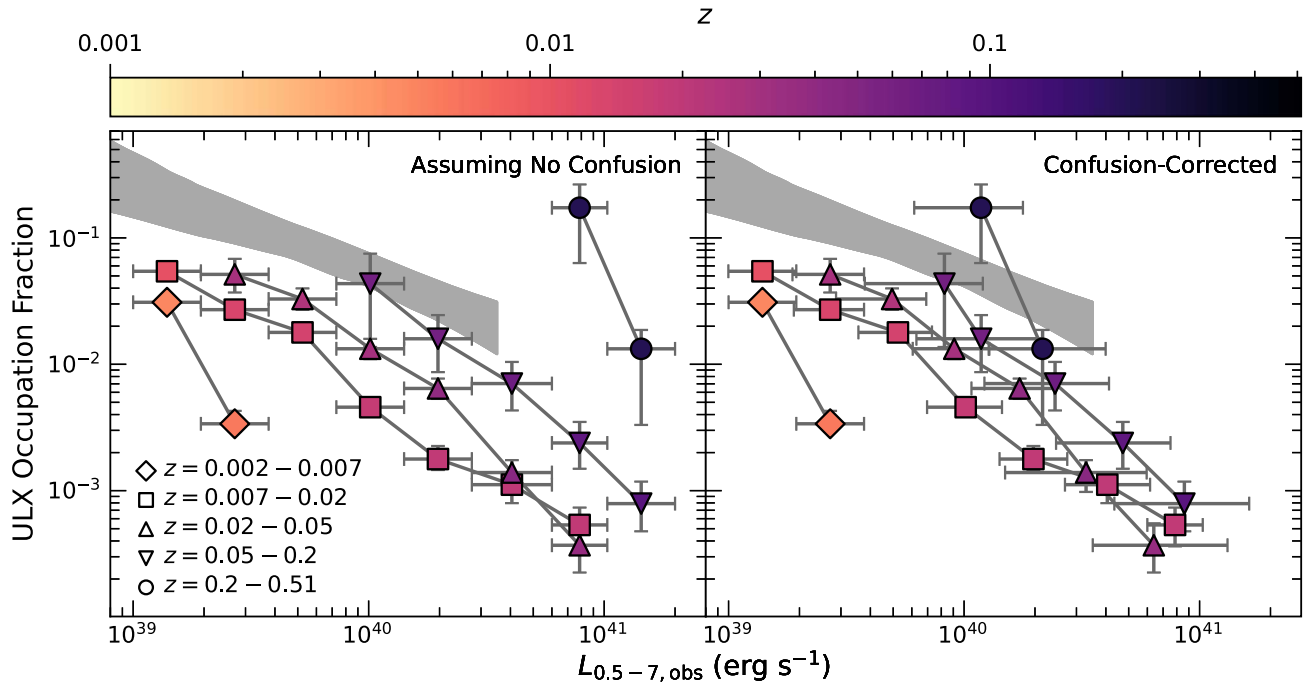


**Figure 13.** ULX occupation fraction against observed 0.5−7 keV luminosity ($L_{0.5-7,\mathrm{obs}}$) in the five redshift bins defined in Figure 4. These fractions are obtained by correcting the observed ULX occupation fraction for spatial resolution (Figure 12), contamination (Section 3), and galaxy inclinations (Section 2.3). The left and right panels, respectively, show fractions without and with corrections for the median estimated number of confused sources applied (see Section 6 for details). The vertical error bars denote the 68.3% confidence intervals (quadrature sum of the binomial bounds, the contamination fraction uncertainties, and the correction factor uncertainties), and the horizontal error bars denote the bin widths (plus the minimum and maximum bounds on the confusion estimates in the right panel). The data points are color-coded according to the median redshift of the ULX candidates in each bin. The gray-shaded region shows the $1\sigma$ bounds on the corrected ULX occupation fraction from the intermediate-redshift sample ($z = 0.038 - 0.298$) of Lehmer et al. (2006).

different samples and X-ray energy ranges used. Moreover, our sample shows that this trend continues until at least $z \sim 0.5$. The confusion-corrected results suggest that the number of galaxies hosting at least one ULX of a given luminosity increases by a factor of $\sim$2 from $z \sim 0.3$ to $z \sim 0.5$, roughly consistent with the corresponding increase in the SFR comoving density over that redshift interval (e.g., Hopkins & Beacom 2006; Madau & Dickinson 2014). In Section 7 we discuss the implications of this evolution on the relation between ULX luminosities and host-galaxy properties. The possibility of accretion onto IMBHs in some cases also remains (though, as stated in Section 5.2, this is not supported by the host-galaxy SED models).

## 7. ULX Contribution to the CXB

While the majority of the CXB is from AGN emission (for a review, see Brandt & Hasinger 2005), the normal galaxy contribution is estimated to be up to $\sim$20% (depending on the energy range and assumptions regarding the X-ray emissivity spectral shape; e.g., Natarajan & Almaini 2000; Hickox & Markevitch 2006; Dijkstra et al. 2012; Lehmer et al. 2012; Aird et al. 2015; Lehmer et al. 2016). In normal galaxies without significant star formation, the X-ray emission is dominated by LMXBs, and at low redshifts, this represents a significant fraction of the total X-ray emission from the normal galaxy population. Toward increasingly higher redshifts, HMXBs begin to dominate the normal galaxy X-ray emission due to the increasing comoving SFR density (peaking at $z \sim 2$; e.g., Hopkins & Beacom 2006; Madau & Dickinson 2014). If ULXs are posited to trace LMXBs and HMXBs, they will likewise contribute significantly to the ionizing radiation output of normal galaxies. However, it is currently unclear how the X-ray background of the ULX population, which represents the luminous end of the XRB luminosity function, evolves with redshift and how closely it follows that of typical XRBs.

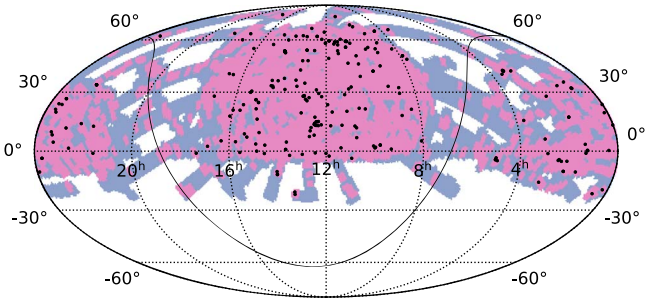


**Figure 14.** Sky map of the SDSS DR16 (gray), the overlapping coverage from the CSC2 (pink), and our individual ULX candidates (black). The map is in equatorial coordinates and shown with a Mollweide projection. The galactic plane is indicated by the solid line.

To constrain this evolution, we first determine the complete overlapping area between the CSC2 and the SDSS footprints (Figure 14). For each ULX candidate in our catalog, we determine the total solid angle of the CSC2–SDSS overlap with a CSC2 0.5−7 keV limiting sensitivity less than or equal to the ULX flux (this corresponds to the total area over which the given ULX could have been detected; e.g., Moretti et al. 2003). As a function of observed 0.5−7 keV flux, we compute the total number of sources (each weighted by the sky area over which it could have been detected). After correcting the numbers for spatial resolution limits (averaged over $L_{0.5-7,\mathrm{obs}} = 10^{39}-2\times10^{41}$ erg s$^{-1}$), contamination (Section 3), and galaxy inclination (Section 2.3), we then divide by the bin size to compute the

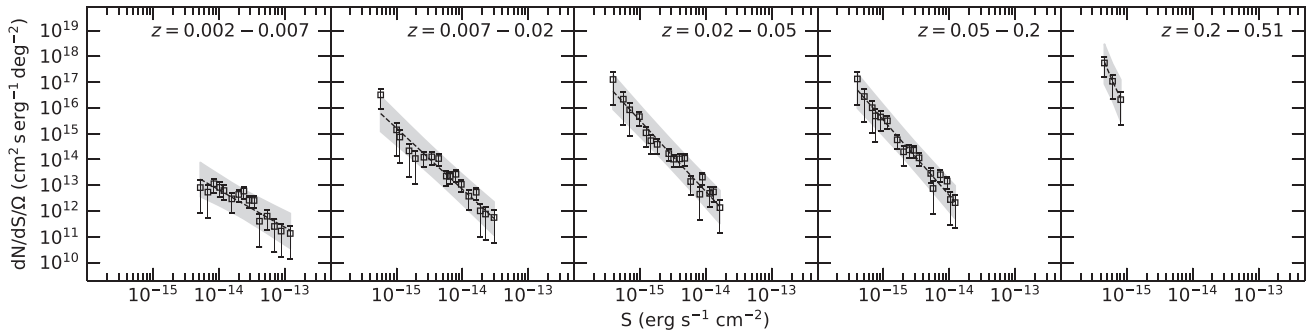


**Figure 15.** Normalized differential source counts ($dN/dS/\Omega$) as a function of flux ($S$) in the redshift bins defined in Figure 4. The counts have been corrected for spatial resolution (Figure 12, averaged over $L_{0.5-7,\mathrm{obs}} = 10^{39}-2\times10^{41}$ erg s$^{-1}$), contamination (Section 3), and galaxy inclination (Section 2.3). The black dashed line is the best-fit power-law function, and the shaded region represents the $3\sigma$ two-sided confidence bounds.

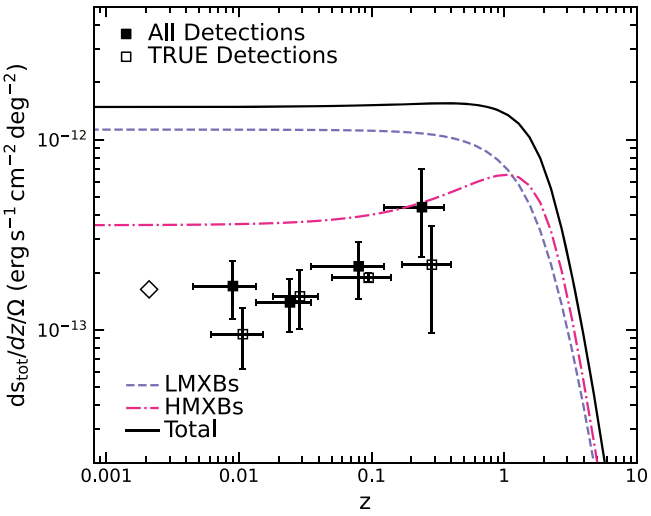


**Figure 16.** Change in normalized flux per unit redshift ($ds_{\mathrm{tot}}/dz/\Omega$) as a function of redshift ($z$) for our full sample of ULX candidates (filled squares) and the subset with `likelihood_class` values of TRUE and without any quality flags set (open squares, horizontally offset for clarity). The vertical error bars indicate the 68.3% confidence intervals, and the horizontal error bars denote the total redshift range of sources contributing to the differential. The individual LMXB and HMXB X-ray point-source contributions (Lehmer et al. 2016) (L16; from detections and stacking) are shown as blue dashed and magenta dotted–dashed lines, respectively, and their sum is shown by the black solid line. For reference, the value from the complete sample of Swartz et al. (2011) (S11; converted to flux per unit solid angle using their sample median redshift) is also shown (open diamond). The X-ray background contribution from our sample of ULXs is consistent with local measurements. At $z\sim0.5$, ULXs account for up to $\sim$ 40% of the total galaxy X-ray background flux.

differential distribution and parameterize it with a power-law function (Figure 15). To obtain the total normalized flux, we integrate the quantity $SdN/dS/\Omega$ over the energy range for which we have measures of the differential distribution.

Figure 16 shows the change in normalized flux per unit redshift of our sample (corrected for the mean fraction of hot ISM gas contribution for our sample in each redshift bin; see Section 2.8). At low redshifts, our estimated value is consistent with that from the local sample of Swartz et al. (2011). We also show the estimated total point-source emission from LMXBs and HMXBs based on X-ray detections and stacking (Lehmer et al. 2016; assuming a Salpeter initial mass function and applying the stellar mass and SFR comoving density from Madau & Dickinson 2014 and $k$-correcting to the observed 0.5−7 keV energy range assuming an X-ray spectral index of $\Gamma = 2.1$). Our results are consistent with the rising contribution from star-forming galaxies as redshift increases and hence with ULXs being predominantly HMXBs. At $z\sim0.5$, the ULXs are potentially consistent with accounting for all of the X-ray flux from HMXBs (i.e., due to star formation). We note, however, that when limiting our sample to CSC2 sources with `likelihood_class` values of TRUE and without any quality flags set (Section 2.7), the contribution per unit redshift is lower by a factor of up to $\sim$2 (Figure 16).

The X-ray flux contribution per unit redshift increases out to $z\sim0.5$ at a rate faster than predicted by the SFR comoving density. Population synthesis models predict that the evolution of XRB X-ray luminosities with SFR is driven by metallicity (e.g., Dray 2006; Linden et al. 2010; Fragos et al. 2013a; Madau & Fragos 2017), and recent observational studies have confirmed this (e.g., Douna et al. 2015; Basu-Zych et al. 2016; Brorby et al. 2016; Fornasini et al. 2020; Ponnada et al. 2020). Therefore, the stronger redshift evolution among our sample (relative to that of typical XRBs) may be caused by a stronger inverse dependence on metallicity, perhaps driven by larger stellar wind strength parameters (e.g., Belczynski et al. 2010) associated with massive donor stars. Alternatively, an increasing association with more massive accretors at higher redshifts may also account for the additional flux. Regardless, at increasingly higher redshifts, a larger fraction of normal galaxy point-source X-ray emission is in the form of intrinsically luminous ULXs (or localized populations of ULXs) and reaches up to $\sim$40% at $z\sim0.5$.

Figure 17 shows how the cumulative ULX contribution to the CXB evolves with redshift and how it compares to the XRB population of normal star-forming galaxies. When integrated out to $z = 0.51$, the total ULX contribution to the CXB is $\sim$1% and consistent with the contribution from star-forming galaxies. If the cumulative ULX contribution follows a similar redshift-dependent trajectory as that of HMXBs out to greater cosmological distances, then ULXs will account for at least $\sim$5% of the total CXB and hence contribute significantly to the overall ionizing flux from galaxies.

## 8. Conclusions

We present a catalog of 259 ULX candidates covering the redshift range $z = 0.002-0.51$ that is constructed by matching SDSS galaxies with the Chandra Source Catalog Version 2. After computing estimates of the relative astrometric accuracy between the SDSS and Chandra images, off-nuclear X-ray sources are identified as those that are spatially offset from the host-galaxy nucleus by >3 times the relative uncertainty in the X-ray and galaxy centroid positions. We further require that the unabsorbed, rest-frame 0.5−7 keV luminosities are above the commonly used lower threshold for ULXs ($10^{39}$ erg s$^{-1}$)

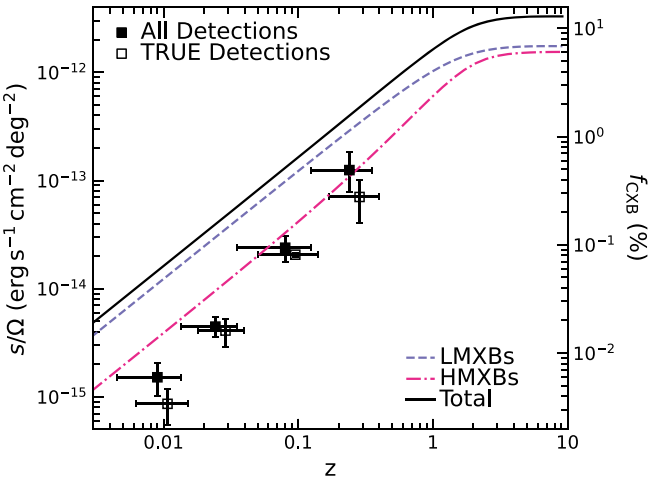


**Figure 17.** Cumulative sum of the normalized 0.5−7 keV flux ($s/\Omega$), computed from the differential values shown in Figure 16. The equivalent percent contribution to the CXB ($f_{\rm CXB}$) is shown on the right ordinate, where the CXB value is the summed soft (0.5–2 keV) and hard (2–8 keV) intensities derived in Lehmer et al. (2012). The vertical error bars indicate the 68.3% confidence intervals (quadrature sum of the binomial bounds, the contamination fraction uncertainties, and the correction factor uncertainties), and the horizontal error bars denote the bin widths. The marker styles and reference curves are the same as in Figure 16. Out to $z = 0.51$, the integrated ULX contribution to the CXB is ∼1% and is expected to be ∼5% if it follows that of star-forming galaxies.

and below the upper threshold set by the most-luminous known accreting compact stellar-mass objects ($2 \times 10^{41}$ erg s$^{-1}$). This catalog includes the largest sample of intermediate-redshift ULX candidates and extends out to higher redshifts than previous samples. We use the large redshift range of the catalog to constrain the physical nature of ULXs by analyzing the redshift evolution of their physical properties, occupation fractions, and contribution to the CXB. Our key conclusions are as follows:

1. The overall contamination fraction is $31\% \pm 4\%$ and shows no evidence for a trend with redshift. Our estimates are consistent with those from previous nearby and intermediate-redshift samples when accounting for the uncertainties.
2. When comparing the ULX candidates to the parent sample, evidence for systematically enhanced sSFRs (at a given stellar mass) is observed. The median value of this offset is $\Delta$sSFR $= 0.48$ dex) and consistent with observations of local ULXs preferentially residing in or near star-forming environments.
3. The sSFRs are statistically consistent with contributions from both LMXBs and HMXBs, though with a systematic bias toward a higher HMXB contribution. The ratios of X-ray luminosity to host-galaxy stellar mass and SFR are consistent with XRB populations at low redshifts (agreement within $0.3\sigma$ and $0.1\sigma$, respectively) but are significantly elevated toward higher redshifts (at the $12\sigma$ and $20\sigma$ levels, respectively). This deviation likely reflects an observational bias toward luminous sources that represent the extreme end of the XRB population and dominate their host-galaxy X-ray emission.
4. The ULX occupation fraction, when corrected for source confusion, is positively correlated with redshift (per luminosity bin), as expected if ULX populations are preferentially found in galaxies with high SFRs and low metallicities. Our estimated occupation fractions are in agreement with previous results and show for the first time a systematic increase from the nearby universe out to $z \sim 0.5$.
5. The integrated contribution to the CXB from ULXs out to $z = 0.51$ is ∼1%. At these redshifts, the ULX X-ray background flux is consistent with that expected from HMXBs and accounts for up to ∼40% of the total normal galaxy X-ray point-source flux. ULXs are therefore likely to contribute significantly to the overall ionizing radiation from galaxies.

We thank an anonymous reviewer for the detailed and insightful comments that have greatly improved the manuscript quality. Support for this work was provided by NASA through Chandra Cycle 20 Proposal No. 20620227 issued by the Chandra X-ray Observatory Center, which is operated by the Smithsonian Astrophysical Observatory for and on behalf of NASA under contract NAS8-03060. The work of DS was carried out at the Jet Propulsion Laboratory, California Institute of Technology, under a contract with NASA. MH is supported by an ESO fellowship. This research has made use of data obtained from the Chandra Source Catalog, provided by the Chandra X-ray Center (CXC) as part of the Chandra Data Archive.

*Facilities:* CXO, GALEX, PS1, Sloan, CTIO:2MASS, FLWO:2MASS, WISE.

*Software:* `Astropy` (Astropy Collaboration et al. 2013, 2018; http://www.astropy.org).

## ORCID iDs

R. Scott Barrows https://orcid.org/0000-0002-6212-7328
Daniel Stern https://orcid.org/0000-0003-2686-9241
Marianne Heida https://orcid.org/0000-0002-1082-7496

## References

Abbott, B. P., Abbott, R., Abbott, T. D., et al. 2016, PhRvL, 116, 061102
Ahumada, R., Prieto, C. A., Almeida, A., et al. 2020, ApJS, 249, 3
Aird, J., Coil, A. L., & Georgakakis, A. 2017, MNRAS, 465, 3390
Aird, J., Coil, A. L., Georgakakis, A., et al. 2015, MNRAS, 451, 1892
Assef, R. J., Stern, D., Noirot, G., et al. 2018, ApJS, 234, 23
Astropy Collaboration, Price-Whelan, A. M., Sipőcz, B. M., et al. 2018, AJ, 156, 123
Astropy Collaboration, Robitaille, T. P., Tollerud, E. J., et al. 2013, A&A, 558, A33
Bachetti, M., Harrison, F. A., Walton, D. J., et al. 2014, Natur, 514, 202
Bachetti, M., Rana, V., Walton, D. J., et al. 2013, ApJ, 778, 163
Barrows, R. S., Comerford, J. M., Greene, J. E., & Pooley, D. 2016, ApJ, 829, 37
Barrows, R. S., Comerford, J. M., Stern, D., & Assef, R. J. 2021, ApJ, 922, 179
Barrows, R. S., Mezcua, M., & Comerford, J. M. 2019, ApJ, 882, 181
Basu-Zych, A. R., Lehmer, B., Fragos, T., et al. 2016, ApJ, 818, 140
Basu-Zych, A. R., Lehmer, B. D., Hornschemeier, A. E., et al. 2013, ApJ, 774, 152
Belczynski, K., Bulik, T., Fryer, C. L., et al. 2010, ApJ, 714, 1217
Bertin, E., & Arnouts, S. 1996, A&AS, 117, 393
Bianchi, L. & GALEX Team 1999, MmSAI, 70, 365
Boquien, M., Burgarella, D., Roehlly, Y., et al. 2019, A&A, 622, A103
Boroson, B., Kim, D.-W., & Fabbiano, G. 2011, ApJ, 729, 12
Brandt, W. N., & Hasinger, G. 2005, ARA&A, 43, 827
Brightman, M., Harrison, F. A., Fürst, F., et al. 2018, NatAs, 2, 312
Brorby, M., Kaaret, P., Prestwich, A., & Mirabel, I. F. 2016, MNRAS, 457, 4081
Bruzual, G., & Charlot, S. 2003, MNRAS, 344, 1000
Chandra, A. D., Roy, J., Agrawal, P. C., & Choudhury, M. 2020, MNRAS, 495, 2664

Colbert, E. J. M., Heckman, T. M., Ptak, A. F., Strickland, D. K., & Weaver, K. A. 2004, ApJ, 602, 231
Colbert, E. J. M., & Ptak, A. F. 2002, ApJS, 143, 25
Comerford, J. M., Pooley, D., Barrows, R. S., et al. 2015, ApJ, 806, 219
Conroy, C., Gunn, J. E., & White, M. 2009, ApJ, 699, 486
Dawson, K. S., Schlegel, D. J., Ahn, C. P., et al. 2013, AJ, 145, 10
Dijkstra, M., Gilfanov, M., Loeb, A., & Sunyaev, R. 2012, MNRAS, 421, 213
Douna, V. M., Pellizza, L. J., Mirabel, I. F., & Pedrosa, S. E. 2015, A&A, 579, A44
Dray, L. M. 2006, MNRAS, 370, 2079
Earnshaw, H. P., Roberts, T. P., Middleton, M. J., Walton, D. J., & Mateos, S. 2019, MNRAS, 483, 5554
Ebisuzaki, T., Makino, J., Tsuru, T. G., et al. 2001, ApJL, 562, L19
Evans, I. N., Primini, F. A., Glotfelty, K. J., et al. 2010, ApJS, 189, 37
Fabbiano, G. 2006, ARA&A, 44, 323
Fabbiano, G., Zezas, A., & Murray, S. S. 2001, ApJ, 554, 1035
Farrell, S. A., Webb, N. A., Barret, D., Godet, O., & Rodrigues, J. M. 2009, Natur, 460, 73
Feng, H., & Kaaret, P. 2009, ApJ, 696, 1712
Fornasini, F. M., Civano, F., & Suh, H. 2020, MNRAS, 495, 771
Fornasini, F. M., Kriek, M., Sanders, R. L., et al. 2019, ApJ, 885, 65
Fragos, T., Lehmer, B. D., Naoz, S., Zezas, A., & Basu-Zych, A. 2013a, ApJL, 776, L31
Fragos, T., Lehmer, B., Tremmel, M., et al. 2013b, ApJ, 764, 41
Fürst, F., Walton, D. J., Harrison, F. A., et al. 2016, ApJL, 831, L14
Gilfanov, M. 2004, MNRAS, 349, 146
Gladstone, J. C., Roberts, T. P., & Done, C. 2009, MNRAS, 397, 1836
Gong, H., Liu, J., & Maccarone, T. 2016, ApJS, 222, 12
Graham, A. W., Driver, S. P., Petrosian, V., et al. 2005, AJ, 130, 1535
Griffith, R. L., Tsai, C.-W., Stern, D., et al. 2011, ApJL, 736, L22
Grimm, H. J., Gilfanov, M., & Sunyaev, R. 2003, MNRAS, 339, 793
Heida, M., Lau, R. M., Davies, B., et al. 2019, ApJL, 883, L34
Heida, M., Torres, M. A. P., Jonker, P. G., et al. 2015, MNRAS, 453, 3510
Hickox, R. C., Jones, C., Forman, W. R., et al. 2009, ApJ, 696, 891
Hickox, R. C., & Markevitch, M. 2006, ApJ, 645, 95
Hinshaw, G., Larson, D., Komatsu, E., et al. 2013, ApJS, 208, 19
Hopkins, A. M., & Beacom, J. F. 2006, ApJ, 651, 142
Hornschemeier, A. E., Alexander, D. M., Bauer, F. E., et al. 2004, ApJL, 600, L147
Hornschemeier, A. E., Heckman, T. M., Ptak, A. F., Tremonti, C. A., & Colbert, E. J. M. 2005, AJ, 129, 86
Inoue, Y., Yabe, K., & Ueda, Y. 2021, PASJ, 73, 1315
Israel, G. L., Belfiore, A., Stella, L., et al. 2017a, Sci, 355, 817
Israel, G. L., Papitto, A., Esposito, P., et al. 2017b, MNRAS, 466, L48
Jonker, P. G., Torres, M. A. P., Fabian, A. C., et al. 2010, MNRAS, 407, 645
Kaaret, P., Feng, H., & Roberts, T. P. 2017, ARA&A, 55, 303
King, A. R., Davies, M. B., Ward, M. J., Fabbiano, G., & Elvis, M. 2001, ApJL, 552, L109
King, A. R., & Dehnen, W. 2005, MNRAS, 357, 275
Kovlakas, K., Zezas, A., Andrews, J. J., et al. 2020, MNRAS, 498, 4790
Lehmer, B. D., Alexander, D. M., Bauer, F. E., et al. 2010, ApJ, 724, 559
Lehmer, B. D., Basu-Zych, A. R., Mineo, S., et al. 2016, ApJ, 825, 7
Lehmer, B. D., Brandt, W. N., Hornschemeier, A. E., et al. 2006, AJ, 131, 2394
Lehmer, B. D., Eufrasio, R. T., Basu-Zych, A., et al. 2021, ApJ, 907, 17
Lehmer, B. D., Xue, Y. Q., Brandt, W. N., et al. 2012, ApJ, 752, 46
Linden, T., Kalogera, V., Sepinsky, J. F., et al. 2010, ApJ, 725, 1984
Liu, J. 2011, ApJS, 192, 10
Liu, J.-F., & Bregman, J. N. 2005, ApJS, 157, 59
Liu, Q. Z., & Mirabel, I. F. 2005, A&A, 429, 1125
López, K. M., Jonker, P. G., Heida, M., et al. 2019, MNRAS, 489, 1249
Luangtip, W., Roberts, T. P., & Done, C. 2016, MNRAS, 460, 4417
Maccarone, T. J., Kundu, A., Zepf, S. E., & Rhode, K. L. 2007, Natur, 445, 183
Madau, P., & Dickinson, M. 2014, ARA&A, 52, 415
Madau, P., & Fragos, T. 2017, ApJ, 840, 39
Mainieri, V., Vignali, C., Merloni, A., et al. 2010, A&A, 514, A85
Mapelli, M., Ripamonti, E., Zampieri, L., Colpi, M., & Bressan, A. 2010, MNRAS, 408, 234
Masini, A., Hickox, R. C., Carroll, C. M., et al. 2020, ApJS, 251, 2
Mezcua, M. 2017, IJMPD, 26, 1730021
Mezcua, M., Civano, F., Fabbiano, G., Miyaji, T., & Marchesi, S. 2016, ApJ, 817, 20
Mezcua, M., Roberts, T. P., Lobanov, A. P., & Sutton, A. D. 2015, MNRAS, 448, 1893
Middleton, M., Done, C., & Schurch, N. 2008, MNRAS, 383, 1501
Middleton, M. J., & King, A. 2017, MNRAS, 470, L69
Miller, M. C., & Hamilton, D. P. 2002, MNRAS, 330, 232
Mineo, S., Gilfanov, M., & Sunyaev, R. 2012, MNRAS, 419, 2095
Montero-Dorta, A. D., Bolton, A. S., Brownstein, J. R., et al. 2016, MNRAS, 461, 1131
Moretti, A., Campana, S., Lazzati, D., & Tagliaferri, G. 2003, ApJ, 588, 696
Motch, C., Pakull, M. W., Soria, R., Grisé, F., & Pietrzyński, G. 2014, Natur, 514, 198
Mukherjee, E. S., Walton, D. J., Bachetti, M., et al. 2015, ApJ, 808, 64
Natarajan, P., & Almaini, O. 2000, MNRAS, 318, L21
Nitz, A. H., Dent, T., Davies, G. S., et al. 2020, ApJ, 891, 123
Noll, S., Burgarella, D., Giovannoli, E., et al. 2009, A&A, 507, 1793
O'Connor, J. A., Rosenberg, J. L., Satyapal, S., & Secrest, N. J. 2016, MNRAS, 463, 811
Pakull, M. W., Soria, R., & Motch, C. 2010, Natur, 466, 209
Pavlovskii, K., Ivanova, N., Belczynski, K., & Van, K. X. 2017, MNRAS, 465, 2092
Plotkin, R. M., Gallo, E., Miller, B. P., et al. 2014, ApJ, 780, 6
Ponnada, S., Brorby, M., & Kaaret, P. 2020, MNRAS, 491, 3606
Poutanen, J., Fabrika, S., Valeev, A. F., Sholukhova, O., & Greiner, J. 2013, MNRAS, 432, 506
Prestwich, A. H., Tsantaki, M., Zezas, A., et al. 2013, ApJ, 769, 92
Ptak, A., & Colbert, E. 2004, ApJ, 606, 291
Ranalli, P., Comastri, A., & Setti, G. 2003, A&A, 399, 39
Remillard, R. A., & McClintock, J. E. 2006, ARA&A, 44, 49
Rémy-Ruyer, A., Madden, S. C., Galliano, F., et al. 2015, A&A, 582, A121
Salpeter, E. E. 1955, ApJ, 121, 161
Scargle, J. D., Norris, J. P., Jackson, B., & Chiang, J. 2013, ApJ, 764, 167
Schreiber, C., Pannella, M., Elbaz, D., et al. 2015, A&A, 575, A74
Scoville, N., Aussel, H., Brusa, M., et al. 2007, ApJS, 172, 1
Scranton, R., Connolly, A. J., Szalay, A. S., et al. 2005, arXiv:astro-ph/0508564
Sigurdsson, S., & Hernquist, L. 1993, Natur, 364, 423
Skrutskie, M. F., Cutri, R. M., Stiening, R., et al. 2006, AJ, 131, 1163
Soria, R., Long, K. S., Blair, W. P., et al. 2014, Sci, 343, 1330
Sutton, A. D., Roberts, T. P., & Middleton, M. J. 2013, MNRAS, 435, 1758
Sutton, A. D., Roberts, T. P., Walton, D. J., Gladstone, J. C., & Scott, A. E. 2012, MNRAS, 423, 1154
Swartz, D. A., Ghosh, K. K., Tennant, A. F., & Wu, K. 2004, ApJS, 154, 519
Swartz, D. A., Soria, R., & Tennant, A. F. 2008, ApJ, 684, 282
Swartz, D. A., Soria, R., Tennant, A. F., & Yukita, M. 2011, ApJ, 741, 49
Swartz, D. A., Tennant, A. F., & Soria, R. 2009, ApJ, 703, 159
Walton, D. J., Fuerst, F., Harrison, F., et al. 2013, ApJ, 779, 148
Walton, D. J., Fürst, F., Heida, M., et al. 2018, ApJ, 856, 128
Walton, D. J., Mackenzie, A. D. A., Gully, H., et al. 2022, MNRAS, 509, 1587
Walton, D. J., Middleton, M. J., Rana, V., et al. 2015, ApJ, 806, 65
Walton, D. J., Roberts, T. P., Mateos, S., & Heard, V. 2011, MNRAS, 416, 1844
Weisskopf, M. C., Tananbaum, H. D., Van Speybroeck, L. P., & O'Dell, S. L. 2000, Proc. SPIE, 4012, 2
Wiktorowicz, G., Lasota, J.-P., Middleton, M., & Belczynski, K. 2019, ApJ, 875, 53
Winter, L. M., Mushotzky, R. F., & Reynolds, C. S. 2006, ApJ, 649, 730
Wolter, A., Trinchieri, G., & Colpi, M. 2006, MNRAS, 373, 1627
Wright, E. L., Eisenhardt, P. R. M., Mainzer, A. K., et al. 2010, AJ, 140, 1868
Zampieri, L., & Roberts, T. P. 2009, MNRAS, 400, 677
Zezas, A., Fabbiano, G., Baldi, A., et al. 2006, ApJS, 166, 211
Zezas, A., Fabbiano, G., Rots, A. H., & Murray, S. S. 2002, ApJS, 142, 239